A wavelet method for the characterization of spatiotemporal patterns

Shuguang Guan [a], C.-H. Lai [a], G.W. Wei [b],*

[a] *Department of Physics, National University of Singapore, Singapore 117543, Singapore*
[b] *Department of Computational Science, National University of Singapore, Singapore 117543, Singapore*

Abstract

This paper introduces a wavelet-based method for the characterization of spatiotemporal patterns. Based on the wavelet multiresolution analysis, two wavelet indices, multiscale accumulative density (MAD) and multiscale accumulative change (MAC), are proposed for the characterization of the dynamics of the spatiotemporal patterns. Both indices are constructed by using orthogonal wavelet projection operators. The MAD is a measure of the spatial complexity of a pattern at a given time, whereas the MAC characterizes the spatial complexity of instantaneous change of the spatiotemporal patterns at a given time. The ratio of the MAD indices between the lowest and the highest scales reflects the order of coherence in a pattern. The time series of both MAD and MAC provide the dynamical information of morphological pattern evolutions. Numerical experiments based on the Cahn–Hilliard equation indicate that the proposed method is efficient for quantitatively characterizing the dynamics of the spatiotemporal patterns. © 2002 Published by Elsevier Science B.V.

PACS: 05.45.-a; 47.54.+r

Keywords: Multiscale accumulative density; Multiscale accumulative change; Cahn–Hilliard equation; Wavelets

1. Introduction

The formation of spatially extended patterns is one of the most fascinating phenomena in nature [1]. The investigation of pattern formation has great impact on many scientific disciplines, including physics, chemistry, biology, materials science and the life sciences. Considerable attention has been drawn to this field in the past few decades. At present, much of our understanding of the dynamics of pattern formation is based on our knowledge of low-dimensional dynamical systems whose dynamics can be well characterized by a few measures, such as the Lyapunov exponents, fractal dimensions and the Kolmogorov–Sinai (KS) entropy [2], etc. However, pattern formation inherently takes place in spatially extended dynamical systems [3,4]. An essential difference between a low-dimensional system and a spatially extended system is the degrees of freedom involved. Due to the large number

of degrees of freedom in spatially extended systems, the characterization of spatiotemporal dynamics remains a major challenge.

Nevertheless, there is a great deal of effort in the characterization of spatiotemporal patterns. Three main classes of methods are developed. The first class of methods attempt to generalize the existing concepts and approaches developed in the low-dimensional dynamical systems. These methods focus on the temporal evolution of the spatiotemporal patterns. The dynamics of the spatially extended systems can be characterized in terms of metric measures of the underlying attractors such as Lyapunov exponents and fractal dimensions. For example, Kaneko [5] proposed several indices, such as co-moving Lyapunov exponents and mutual information for the quantitative characterization of spatiotemporal dynamics based on the coupled map lattices (CML) models. Several other invariant measures have also been proposed, including Lyapunov dimension density [6–9,13], Karhunen–Loéve decomposition density [10], finite-time dimension density [11], the KS entropy [12] and KS entropy density [7,13]. Among them, the Lyapunov dimension density is frequently used. However, it is well known that the accurate numerical computation of the Lyapunov spectrum for spatially extended dynamical systems is usually difficult and expensive in terms of computer resources. For this reason, several methods have been proposed to estimate the attractor dimension of spatially extended systems [14–16].

The second class of methods utilize the linear decomposition of the spatiotemporal patterns in terms of a set of (known) spatial modes. The most commonly used spatial modes include Fourier modes and Karhunen–Loéve (KL) modes. The Fourier modes are orthogonal and complete for describing the ordered state patterns. However, the expansion in Fourier modes might suffer from slow convergence for sharply varying systems which may excite thousands of Fourier modes. The KL modes, obtained by using the KL decomposition [17,18], can be regarded as a set of special bases. The essence of the KL decomposition is to find a minimal set of spatial modes that can be used to provide a good approximate description of the ordered state patterns, as well as the essential information about the dynamics of the system [19]. Stone and Cutler [20] have extended the KL decomposition to the archetypal analysis and used it to analyze spatiotemporal dynamics. The advantage of KL modes is that they are adapted to the spatiotemporal patterns under consideration. However, the computation of KL modes for a spatiotemporal system is often time-consuming, particularly, if the spatial field or the temporal evolution of the system is recorded at a high resolution.

The third kind of methods attempt to draw analogies to thermodynamic and statistical systems. For example, thermodynamic formalism characterizes the spatiotemporal dynamics by using certain appropriately defined thermodynamic functions [21,22]. Many other useful statistical approaches were proposed, including spectra entropy [23,24], correlation length [25,26], coherent clusters [27], structure factor [28–30], and local pattern properties [31].

At present, linear decomposition methods are frequently used for analyzing spatiotemporal patterns (or spatiotemporal time series), especially in the "small system" regime where the system size is comparable with the typical correlation length of the system [3]. In this regime, due to the dissipation and coupling among different degrees of freedom, it is possible that most degrees of freedom are either "dissipated" (in self-organization language) or "enslaved" (in synergetic language) by a few dominant degrees of freedom. Physically, this corresponds to the formation of spatially coherent structures or patterns [3]. In this case, the temporal complexity and the spatial complexity in the spatially extended systems are relatively independent of each other. In general, if there are only a few dominant spatial modes in the system, then the dynamics of the system can be effectively reduced and characterized by the temporal evolutions of these few dominant modes [32]. The mode decomposition approach is generally efficient only if the attractor of the spatially extended system is actually low-dimensional. However, in some cases, even if the spatiotemporal dynamics is governed by a low-dimensional attractor, the spatial mode decomposition might still not be efficient because of the incompatibility between the mode basis and the physical system under investigation [39,40]. Moreover, in many cases, the modal decomposition shows that the total energy may distribute over a large number of spatial modes and then linear decomposition methods lose their efficiency and become inapplicable.

Therefore, it remains a challenging task to characterize the temporal evolution of spatiotemporal patterns under such circumstance.

Recently, we utilized a Fourier–Bessel decomposition method for the characterization of spatiotemporal patterns simulated in a circular domain [33]. A series of spatiotemporal patterns have been observed by using the Cahn–Hilliard equation as a theoretical model. It is found that the pattern morphology can be controlled by the boundary conditions and the geometric size of the circular domain [34]. Theoretical analysis revealed that for a small geometric domain, the ordered state patterns can be efficiently decomposed as a linear combination of Fourier–Bessel modes. For example, for the ordered state pattern shown in Fig. 1(a), Fourier–Bessel decomposition demonstrates that there are only three active modes which capture 99% pattern energy (defined as the total Fourier–Bessel decomposition amplitudes), as shown in Fig. 1(c). Among them the principal mode [1,4] is the dominant one which contributes most to the pattern morphology. In this "small system" regime, the Fourier–Bessel decomposition method provides an efficient characterization to the rich morphological evolutions observed in the circular domain, including steady states, uniform oscillations, modulated oscillations and chaotic dynamics. However, the method becomes less efficient as the geometric domain increases. In such a case, the number of Fourier–Bessel modes that can be simultaneously excited at certain control parameter becomes large, and the spatially coherent structures are easily destroyed by the simultaneous excitation and competition of multiple Fourier–Bessel modes. As a consequence, the dynamics of the system is no longer dominated by a few Fourier–Bessel modes. Fig. 1(b) shows a pattern observed at a moderately large control parameter. The Fourier–Bessel decomposition in Fig. 1(d) demonstrates that the total energy of the pattern distributes over a large number of Fourier–Bessel modes rather than a few principal ones as shown in Fig. 1(c). There are a total of 21 modes whose decomposition amplitudes are greater than 0.01. It can be expected that with the further increase in the control parameter, it is impossible to track the dynamics of a large number of active modes. Therefore the Fourier–Bessel decomposition method is no longer efficient to characterize the temporal evolution of the spatiotemporal patterns in moderately large and large domains.

The purpose of the present work is to develop an alternative and more effective approach for resolving the above mentioned difficulty in the characterization of the spatiotemporal patterns. To this end, we make the use of wavelet analysis and its associated time–frequency multiresolution technique for spatiotemporal pattern dynamics. Basically, the spatial pattern can be decomposed in the wavelet space according to different frequency sub-bands. The relative wavelet energy at different frequency sub-bands can be used as an index to characterize the dynamics of the spatiotemporal patterns. Fig. 1(e) and (f) illustrate the relative wavelet energy of the three high frequency scales, which are obtained by the three-scale wavelet multiresolution analysis of Fig. 1(a) and (b). The use of wavelet decompositions as a characterization of nonlinear pattern dynamics is addressed.

Wavelet analysis is a powerful mathematical tool and has had tremendous success in telecommunication, signal/image processing, image compression, and artificial intelligence. Wavelet multiresolution analysis has also found its applications in the study of nonlinear dynamical systems. These include time series analysis [35–37], recognition and noise filtering [38], low-dimensional dynamical prediction [40], and turbulence analysis [41–44]. It is believed that wavelet analysis may play an important role in the study of pattern formation [1]. In a more general sense, three-dimensional wavelet-based techniques have been successfully used in the field of spatiotemporal (i.e., three-dimensional) image compression [45–49]. By constructing appropriate multiresolution wavelet filter, e.g., the adaptive motion-compensated filters, the correlated spatiotemporal features such as optical flow can be effectively encoded so that the motion and structure of the moving objects in a three-dimensional video image can be extracted base on their location, size and speed. In the present study, a method based on wavelet multiresolution is developed. Our primary concern here is to characterize the temporal evolution of spatiotemporal patterns in the small and moderately large spatially extended systems. In particular, we need to extract the time series which can be used to characterize the dynamics of the spatiotemporal patterns in terms of periodic or chaotic evolution, etc. Obviously,
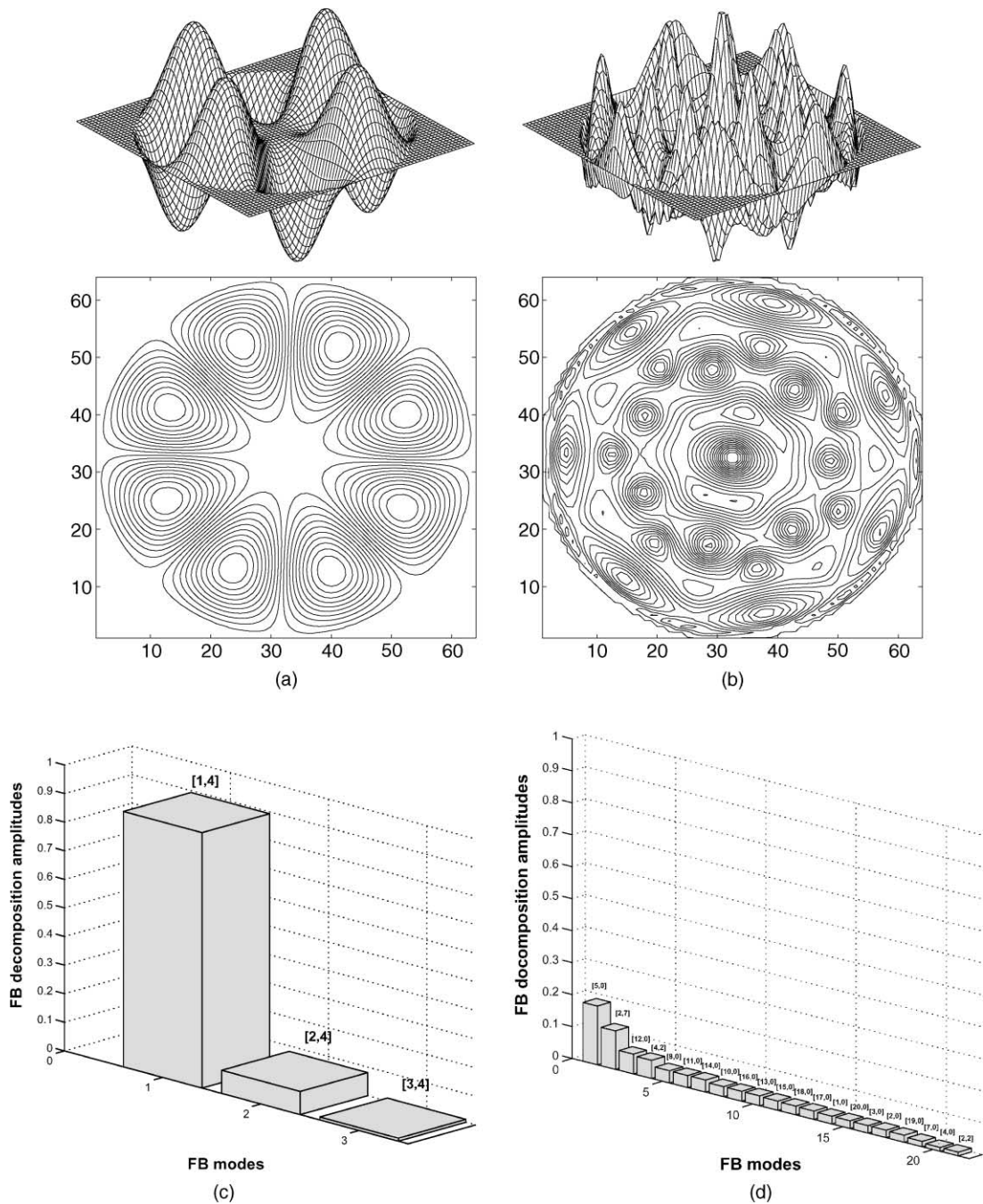
Fig. 1. (a) A typical pattern at $R = 7.5$; (b) a typical pattern at $R = 13.5$; (c) Fourier–Bessel decomposition of pattern (a); (d) Fourier–Bessel decomposition of pattern (b); (e) wavelet decomposition of pattern (a); (f) wavelet decomposition of pattern (b).
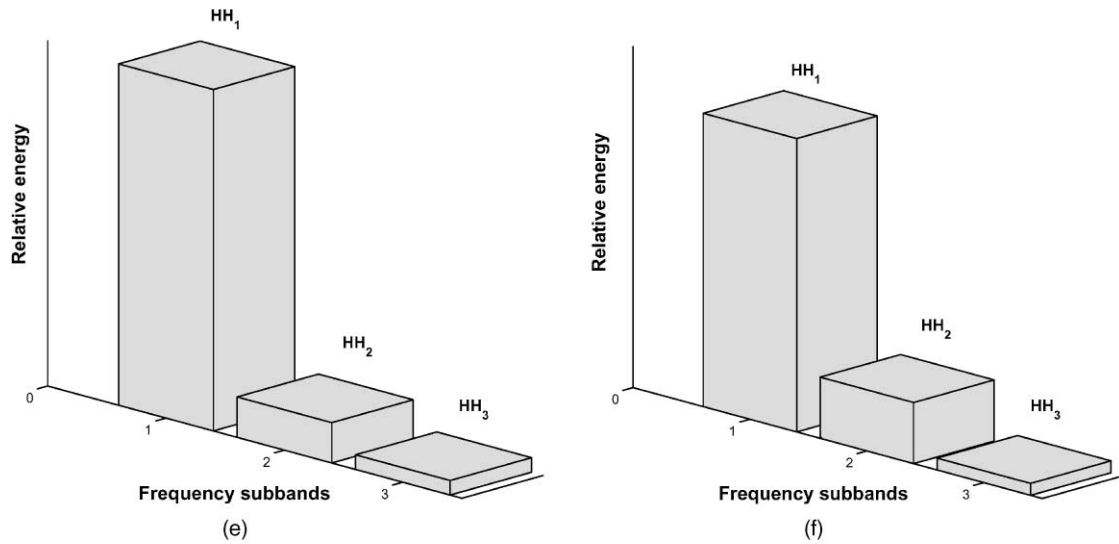
Fig. 1. (*Continued*).

our use of wavelets for nonlinear dynamics is different from that for the video image compression or pattern recognition. Form the dynamical system point of view, the system considered in our study is entirely deterministic and it is governed by a nonlinear partial differential equation. In certain sense, the dynamics governed by a nonlinear partial differential equation might be relatively simpler compared with the three-dimensional video images which are often unpredictable and very complicated. Therefore, video image characterization and tracking require a larger set of physical observables (including the optical flow). As a result, wavelet algorithms used in video images are often more sophisticated.

The rest of the paper is organized as the follows. A wavelet-based method for pattern analysis and characterization is introduced in Section 2. A brief review of the wavelet theory is given as a background before we introduce our approach. Two wavelet indices, a normalized multiscale accumulative density (MAD) and a normalized multiscale accumulative change (MAC), are proposed for the dynamical characterization of the morphological evolution of spatiotemporal patterns. In Section 3, we apply the present wavelet methods to the spatiotemporal patterns obtained by integrating the Cahn–Hilliard equation in a circular domain. This paper ends with a conclusion.

2. Theory and method

2.1. Theoretical background

The theory of wavelets, including frames, is a new branch of mathematics developed in the last two decades and has been widely applied in a variety of engineering and science disciplines [50–54]. Mathematically, wavelet and frame systems are sets of L^2 functions generated from a single function by two elementary operations, translation and dilation. Compared to usual orthogonal L^2 bases, wavelet and frame systems often have much better properties for expanding an L^2 function of a physical origin. Physically, wavelet transform can split a signal into different frequency bands or components so that each component can be studied with a resolution matched to its scale, thus providing excellent frequency and spatial resolution, and achieving high computational efficiency. One

of the most important properties of wavelet and frame on $L^2(\mathbf{R})$ is that they can be simultaneously smooth and decaying in both the position and momentum representations. What is equally important is the multiresolution property. Hence, one can devise such an $L^2(\mathbf{R})$ system for representing physical information at various levels of details, leading to the so-called mathematical microscopy. For these reasons, wavelet, frame and their associated multiresolution analysis have been successfully used in a variety of telecommunication and engineering fields, such as data compression, signal processing and image processing. For many physical systems, due to the multiscale nature, wavelet multiresolution theory provides perhaps some of the most appropriate analysis tools. For example, wavelet analysis has been used to analyze fractals and their associated dynamics. Moreover, wavelet packets are found useful for local characterization of classic turbulence and for pattern recognition. In the field of pattern formation, due to the multiscale nature of patterns, wavelet transform is regarded as "the bridge between theory and experiment" [1]. It not only allows us to extract physical information from experimental and computational patterns, but also provides us a convenient method to detect and locate pattern defects. In this study, we use wavelet multiresolution to analyze the ordered state patterns and to characterize the morphological evolution of spatiotemporal patterns.

An orthogonal wavelets system is usually generated from a single function, either a scaling function (father wavelet) ϕ or a mother wavelet ψ, by standard translation and dilation technique

$$\phi_{m,n}(x) = 2^{m/2}\phi(2^m x - n), \quad m, n \in Z, \tag{1}$$

$$\psi_{m,n}(x) = 2^{m/2}\psi(2^m x - n), \quad m, n \in Z, \tag{2}$$

where symbol Z denotes the set of all integers. This can be rephrased in terms of a multiresolution analysis, i.e., a nested sequences of closed subspace $\{V_m\}_{m\in Z}$ such that

1. $\{\phi(x - n)\}$ is an orthogonal basis of V_0;
2. $\cdots \subset V_{-1} \subset V_0 \subset V_1 \subset \cdots \subset L^2(\mathbf{R})$;
3. $f(x) \in V_m \Leftrightarrow f(2x) \in V_{m+1}$;
4. $\cap_m V_m = \{0\}$ and $\overline{\cup_m V_m} = L^2(\mathbf{R})$.

Since $\phi \in V_0 \subset V_1$, it must have an expansion in $\{\phi_{1,n} = 2^{1/2}\phi(2x - n)\}$, which is an orthonormal basis for V_1

$$\phi(x) = \sum_n c_n \phi_{1,n}, \tag{3}$$

where $\{c_n\}$ is a set of finite coefficients.

For an orthogonal system, the subspace V_1 can be further split into its orthogonal projection in V_0 and its orthogonal complementary W_0

$$V_1 = V_0 \oplus W_0, \tag{4}$$

where W_0 is a subspace spanned by mother wavelets $\{\psi\}$. If such ψ can be found, then

$$\psi_{m,n}(x) = 2^{m/2}\psi(2^m x - n), \quad m, n \in Z \tag{5}$$

is an orthonormal basis of W_m. Furthermore,

$$\oplus_{m\in Z} W_m = L^2(\mathbf{R}), \tag{6}$$

and thus $\{\psi_{m,n}\}$ ($m, n \in Z$) is an orthonormal basis of $L^2(\mathbf{R})$. Similar to Eq. (3), the mother wavelet can also be expanded as a superposition of $\{\phi_{1,n}\}$

$$\psi(x) = \sum_n c_{1-n}(-1)^n \phi_{1,n}, \tag{7}$$

where $\{c_n\}$ are expansion coefficients.

For the purpose of multiresolution analysis, we define orthogonal subspace projectors

$$\mathcal{V}_m = \sum_{n \in Z} |\phi_{m,n}\rangle \langle \phi_{m,n}|,$$

where the projector $\mathcal{V}_m$ has its domain in $L^2(\mathbf{R})$ and its range in the subspace V_m. For an arbitrary function $f \in L^2(\mathbf{R})$, the projector $\mathcal{V}_M$ selects out the component belonging to subspace V_M

$$\mathcal{V}_M f = (\mathcal{V}_M f - \mathcal{V}_{M-1} f) + \cdots + (\mathcal{V}_1 f - \mathcal{V}_0 f) + \mathcal{V}_0 f = \mathcal{V}_0 f + \sum_{m=0}^{M-1} \mathcal{W}_m f, \tag{8}$$

where

$$\mathcal{W}_m = \mathcal{V}_{m+1} - \mathcal{V}_m = \sum_{n \in Z} |\psi_{m,n}\rangle \langle \psi_{m,n}|$$

is the orthogonal projector from $L^2(\mathbf{R})$ onto the subspace W_m, i.e., the wavelet space at a certain scale m. At a certain specific scale m, we have

$$\mathcal{W}_m f = \sum_{n \in Z} \langle \psi_{m,n} | f \rangle | \psi_{m,n} \rangle = \sum_{n \in Z} d_{m,n} | \psi_{m,n} \rangle, \tag{9}$$

and

$$\mathcal{V}_m f = \sum_{n \in Z} \langle \phi_{m,n} | f \rangle | \phi_{m,n} \rangle = \sum_{n \in Z} c_{m,n} | \phi_{m,n} \rangle. \tag{10}$$

Here, the coefficients $\{d_{m,n}\}$ contain the information for the details (high-pass part) of f at scale m while $\{c_{m,n}\}$ contain the information for a rough approximation (low-pass part) of f at scale m. These two sets of coefficients are related recursively through fast wavelet transform.

So far the simplest example of wavelets is the Haar's wavelets system [54], which is obtained by the dilation and translation of $\phi(x) = \chi_{[0,1)}(x)$, the characteristic function of interval $[0, 1)$. Here, $\phi(x)$ obviously has orthogonal translations. The dilation of ϕ results in characteristic functions for smaller (or larger) intervals and each of them spans a subspace V_m by translations. Haar's wavelets play an important role in the wavelet theory and application for their simplicity.

It is not obvious that a multiresolution analysis exists for ϕ other than the Haar system. The construction of the first few orthogonal wavelet bases was more or less an art rather than a procedure. This requires ingenuity, special tricks and subtle computations. One procedure used by Meyer [50] is to start with a spline function $\theta(x) = (1 - |x - 1|)\chi_{[0,2]}$ which, by translations, spans a non-orthogonal Riesz basis (a frame of the least redundant possible). The corresponding wavelet basis $\{\phi\}$ is obtained in the Fourier space by making the use of orthonormality and periodicity. Daubechies [51] presented another scheme for constructing orthogonal wavelets. In her scheme, the use is made for the dilation relation, together with the orthonormality and periodicity, to determine a wavelet basis in the Fourier representation.

Apart from the Haar system, it is generally true that no other wavelet system can be simultaneously compactly supported, orthogonal and linear phase for its corresponding quadratic mirror filter [51]. A compromise approach is to construct a biorthogonal wavelet system [52] which is both compactly supported and linear phase. Like orthogonal wavelets, biorthogonal wavelets can be used for perfect reconstruction and are very powerful for various applications.

2.2. Wavelet pattern analysis

Spatiotemporal patterns can be described by a scalar field $f(\mathbf{r}, t) \in L^2(\mathbf{R}^3)$. Here $\mathbf{r}$ is a two-dimensional position vector and t is the time. In this study, we assume that spatiotemporal patterns are either a set of discrete experimental patterns or a series of computer simulated patterns $f(x_i, y_j, t_k), i, j \in Z, k \in Z^+$, which can be regarded as a series of "images" in terms of digital image processing. In order to analyze the spatial patterns, without the loss of generality, we consider a two-variable wavelet multiresolution analysis (WMA) in $L^2(\mathbf{R}^2)$. The latter is used to analyze the two-dimensional ordered state patterns in Section 3. In general, the $L^2(\mathbf{R}^2)$ space can be constructed as a tensor product of two $L^2(\mathbf{R})$ subspaces.

Let $\{V_m^i\}_{m \in Z}(i = x, y)$ of $L^2(\mathbf{R})$ be the subspace sequences in the one-dimensional MRA, we define

$$S_m = V_m^x \otimes V_m^y, \quad m \in Z \tag{11}$$

as the sequence of embedded subspaces in $L^2(\mathbf{R}^2)$. Then the two-dimensional MRA can be expressed as follows:

1. $f(x, y) \in S_0 \Leftrightarrow f(x - n, y - l) \in S_0 \ \forall n, l \in Z$;
2. $\cdots \subset S_{-1} \subset S_0 \subset S_1 \subset \cdots \subset L^2(\mathbf{R}^2)$;
3. $f(x, y) \in S_m \Leftrightarrow f(2x, 2y) \in S_{m+1}, m \in Z$;
4. $\cap_{m \in Z} S_m = \{0\}$ and $\overline{\cup_{m \in Z} S_m} = L^2(\mathbf{R}^2)$.

According to the one-dimensional MRA, we have

$$V_{m+1}^i = V_m^i \oplus W_m^i, \quad i = x, y. \tag{12}$$

Therefore, two-dimensional subspaces can be divided into

$$S_{m+1} = V_{m+1}^x \otimes V_{m+1}^y = [V_m^x \oplus W_m^x] \otimes [V_m^y \oplus W_m^y] = S_m \oplus S_m^{LH} \oplus S_m^{HL} \oplus S_m^{HH}, \tag{13}$$

where $S_m \equiv S_m^{LL} = V_m^x \otimes V_m^y, S_m^{LH} = V_m^x \otimes W_m^y, S_m^{HL} = W_m^x \otimes V_m^y$ and $S_m^{HH} = W_m^x \otimes W_m^y$. Here, L and H resemble "low-pass" and "high-pass", respectively. Appropriate basis functions for each wavelet subspace can be constructed as the product of the one-dimensional basis functions, e.g.,

$$\Psi_{m,n,l}^{\alpha\beta} = \begin{cases} \psi_{m,n}^x \psi_{m,l}^y, & \alpha = H, \ \beta = H, \\ \phi_{m,n}^x \psi_{m,l}^y, & \alpha = L, \ \beta = H, \\ \psi_{m,n}^x \phi_{m,l}^y, & \alpha = H, \ \beta = L, \\ \phi_{m,n}^x \phi_{m,l}^y, & \alpha = L, \ \beta = L \end{cases} \quad (n, l, m \in Z), \tag{14}$$

where $\psi^i (i = x, y)$ are the wavelet functions corresponding to the one-dimensional MRA generated by the scaling function $\phi^i (i = x, y)$. Here, $\{\Psi_{m,n,l}^{HH}\}$, $\{\Psi_{m,n,l}^{LH}\}$, $\{\Psi_{m,n,l}^{HL}\}$ and $\{\Psi_{m,n,l}^{LL}\}$ are the orthonormal bases in the subspaces $S_m^{HH}, S_m^{LH}, S_m^{HL}$ and S_m^{LL}, respectively. Example applications of wavelet pattern analysis will be given in Section 3.

2.3. Wavelet pattern characterization

The concept of pattern characterization differs from that of pattern analysis. In pattern analysis, usually there is no information loss in the representation of the original pattern. The commonly used analysis tools include Fourier transform, wavelet transform, Wigner transform, Z transform and KL decomposition. For each of these methods, there is a perfect reconstruction transform (inverse transform). This implies that there is no loss of information in the transform process. In practice, we are facing the difficulty of handling enormously large pattern data sets of

the order of 10^8 points. Our task is to extract useful dynamical information about pattern formation and evolution from these huge data sets. The success of any potential method relies on its ability in the reduction of the spatially extended data of the order 10^4 into a set of reduced indices which can reflect the spatial complexity and the dynamics of the original spatiotemporal system. Therefore, pattern characterization methods provide a reduced representation of the original pattern and there is an irreversible information loss in association with the characterization process. A successful characterization method should be able to select out the essential information of interest by using a minimum set of quantitative indices. To this end, we introduce a wavelet multiresolution framework as a measure for pattern characterization.

In order to extract the detailed information of a spatial pattern in a certain frequency sub-band, we define four projection operators which project a two-dimensional pattern $f(x, y) \in L^2(\mathbf{R}^2)$ onto subspaces S_m, S_m^{HH}, S_m^{LH} and S_m^{HL}, i.e.,

$$\mathcal{S}_m^{\alpha\beta} = \sum_{n,l \in Z} |\xi_{m,n}^{x\alpha} \xi_{m,l}^{y\beta}\rangle \langle \xi_{m,n}^{x\alpha} \xi_{m,l}^{y\beta}|, \tag{15}$$

where $\alpha, \beta \in \{L, H\}$ and

$$\xi_{m,n}^{i\gamma} = \begin{cases} \phi_{m,n}^i, & \gamma = L, \ i = x, y, \\ \psi_{m,n}^i, & \gamma = H, \ i = x, y. \end{cases}$$

The project operator of a given wavelet subspace has a multiresolution decomposition

$$\mathcal{S}_M = \oplus_{\alpha,\beta \in \{L,H\}} \mathcal{S}_{M-1}^{\alpha\beta} = \mathcal{S}_0 \oplus \sum_{m=0}^{M-1} \mathcal{S}_m^{\mathrm{HH}} \oplus \sum_{m=0}^{M-1} \mathcal{S}_m^{\mathrm{LH}} \oplus \sum_{m=0}^{M-1} \mathcal{S}_m^{\mathrm{HL}}, \tag{16}$$

where $\mathcal{S}_M \equiv \mathcal{S}_M^{\mathrm{LL}}$. Obviously, the summation of wavelet projections gives arise to the resolution identity $\mathcal{I}$ in $L^2(\mathbf{R}^2)$

$$\oplus_{m,\alpha,\beta}' \mathcal{S}_m^{\alpha\beta} = \mathcal{I}, \quad \alpha, \beta \in \{H, L\}, \ m \in Z, \tag{17}$$

where the summation excludes all $\alpha = \beta = L$.

The notation of the two-dimensional WMA is schematically shown in Fig. 2(a) with $M = 3$. After three-scale two-dimensional WMA, the two-dimensional spatial pattern can be decomposed into different frequency sub-bands. The upper left square labeled by LL_1 corresponds to the lowest frequency sub-band in both the horizontal and vertical directions, as shown in Fig. 2(a). The information contained in this sub-band is a coarse approximation of the original pattern. The other nine regions involve higher frequency sub-bands and they contain the details of the original pattern at different scales. Among them, the three diagonal regions labeled by HH_3, HH_2, HH_1 correspond to the highest frequency sub-band at each scale and they contain the most detailed information of the original pattern in their scale.

An image or a pattern is a square integrable function that can be decomposed into appropriate subspace components by means of the projection operator

$$f_m^{\alpha\beta} = \mathcal{S}_m^{\alpha\beta}|f\rangle = \sum_{n,l \in Z} |\xi_{m,n}^{x\alpha} \xi_{m,l}^{y\beta}\rangle \langle \xi_{m,n}^{x\alpha} \xi_{m,l}^{y\beta}|f\rangle = \sum_{n,l \in Z} d_{m,n,l}^{\alpha\beta} |\xi_{m,n}^{x\alpha} \xi_{m,l}^{y\beta}\rangle, \tag{18}$$

where $\{d_{m,n,l}^{\alpha\beta}\}$ are the decomposition coefficients. Each component, $f_m^{\alpha\beta}$, provides a mathematical microscopy of the pattern f in an appropriate frequency sub-band. The larger the m value, the higher frequency the sub-band is. Physically, high frequency sub-band is associated with the variance or the "edge" of the pattern under study. For example, noisy or irregular patterns, texture image, and turbulence flow field have large frequency responses at high frequency sub-bands. In contrast, smooth pattern, soft-tissue image, and laminar flow field have relatively small

(a)

(1)

(2)

(3)
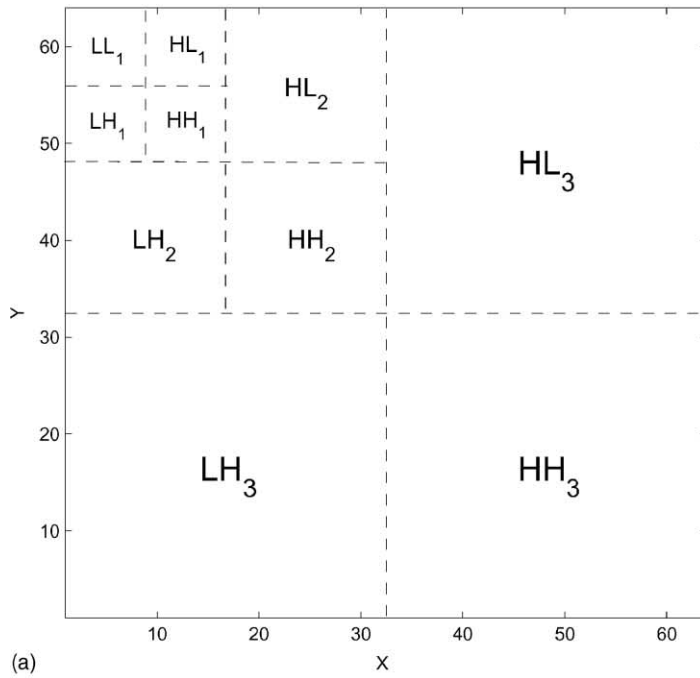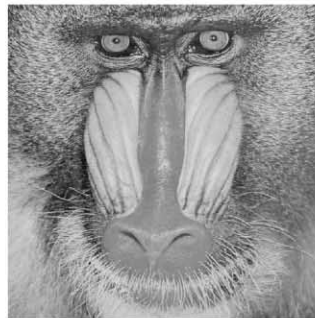
(b) (4)

Fig. 2. (a) Sub-bands of the three-scale wavelet transform. (b) Standard images: (1) Pepper; (2) Lena; (3) Barbara and (4) Mandrill.

frequency responses at high frequency sub-bands. Based on this observation, we propose to use the MAD at each given scale m as a quantitative measure to assess the spatial complexity of pattern $f(x, y, t_i)$ at a given time t_i

$$
\begin{aligned}
\rho^{\alpha\beta m}(t_i) = \|f_m^{\alpha\beta}(t_i)\|^2 &= \left\| \sum_{n,l\in Z} |\xi_{m,n}^{x\alpha}\xi_{m,l}^{y\beta}\rangle\langle\xi_{m,n}^{x\alpha}\xi_{m,l}^{y\beta}|f(t_i)\rangle \right\|^2 \\
&= \sum_{n,l\in Z}\sum_{n',l'\in Z} d_{m,n,l}^{\alpha\beta}(t_i)[d_{m,n',l'}^{\alpha\beta}(t_i)]^*\langle\xi_{m,n'}^{x\alpha}\xi_{m,l'}^{y\beta}|\xi_{m,n}^{x\alpha}\xi_{m,l}^{y\beta}\rangle \\
&= \sum_{n,l\in Z}\sum_{n',l'\in Z} d_{m,n,l}^{\alpha\beta}(t_i)[d_{m,n',l'}^{\alpha\beta}(t_i)]^*\delta_{n,n'}\delta_{l,l'} = \sum_{n,l\in Z} |d_{m,n,l}^{\alpha\beta}(t_i)|^2,
\end{aligned} \tag{19}
$$

where the $*$ denotes the complex conjugate. Using the resolution identity, Eq. (17), the total density of the pattern $f(x, y, t)$ is given by

$$
\|f\|^2 = \sum_{m\in Z}\sum_{\alpha,\beta\in\{L,H\}}^{\prime} \|f_m^{\alpha\beta}\|^2. \tag{20}
$$

Here, the summation $\sum_{\alpha,\beta\in\{L,H\}}^{\prime}$ excludes $\alpha = \beta = L$. It is more appropriate to define a normalized MAD as

$$
\rho_{\text{MAD}}^{\alpha\beta m}(t_i) = \frac{\|f_m^{\alpha\beta}(t_i)\|^2}{\|f\|^2} = \sum_{n,l\in Z} \frac{|d_{m,n,l}^{\alpha\beta}(t_i)|^2}{\|f\|^2}. \tag{21}
$$

The MAD of a given pattern is a positive definite number for a given scale m. Obviously, an irregular pattern has a larger MAD value than that of a smooth one. Hence, the value of MAD, or the "MADness", is a characteristic of spatial complexity for a given spatial pattern at a given time. In ordinary situations, the MAD provides a good description of a spatiotemporal system as a function of time. Fig. 2(b) depicts standard patterns, e.g., Peppers, Lena, Barbara and Mandrill images. In Table 1, we list their MAD indices. For simplicity, as shown in Fig. 2(a), we denote the MAD indices by abbreviation $\text{HH}_m(t_i) = \rho_{\text{MAD}}^{\text{HH}m}(t_i)$ throughout this paper. Generally, it is found that the MAD indices of the Barbara and Mandrill are larger than that of the Peppers and Lena. This is reasonable because the Barbara and Mandrill have more high frequency response than that of the Peppers and Lena.

   An efficient algorithm used in a video compression is to encode the difference of each two successive time steps at each spatial location. Such an approach can greatly increase the compression ratio and peak signal to noise ratio. Similarly, this idea can be utilized in the characterization of spatiotemporal systems. Let us define a new scalar field

Table 1
The MAD indices of some standard images

MAD index	Pepper	Lena	Barbara	Mandrill
HH_3	0.103E − 3	0.769E − 4	0.638E − 3	0.174E − 2
LH_3	0.137E − 2	0.854E − 3	0.103E − 1	0.300E − 2
HL_3	0.953E − 3	0.291E − 3	0.632E − 3	0.888E − 2
HH_2	0.309E − 3	0.426E − 3	0.160E − 2	0.240E − 2
LH_2	0.191E − 2	0.200E − 2	0.344E − 2	0.340E − 2
HL_2	0.166E − 2	0.798E − 3	0.123E − 2	0.686E − 2
HH_1	0.864E − 3	0.102E − 2	0.507E − 3	0.191E − 2
LH_1	0.484E − 2	0.421E − 2	0.354E − 2	0.311E − 2
HL_1	0.351E − 2	0.130E − 2	0.204E − 2	0.361E − 2
LL_1	0.984	0.990	0.976	0.965

as the difference of two successive values of the function f

$$\delta f(x, y, t_i) = f(x, y, t_{i+1}) - f(x, y, t_i). \tag{22}$$

Note that, at the limit of $\Delta t = t_{i+1} - t_i \to 0$, $\delta f(x, y, t_i)/\Delta t$ gives rise to the rate of change of a pattern at time t_i. Hence, $\delta f(x, y, t_i)$ provides the information of the temporal change of the spatiotemporal patterns. Such dynamical change is especially important in the spatiotemporal intermittency. However, for spatially extended systems, it is too expensive to track all the time series at each location. Instead, to characterize the dynamical change, we define a normalized MAC as

$$\rho_{\text{MAC}}^{\alpha\beta m}(t_i) = \frac{\|(\delta f)_m^{\alpha\beta}(x, y, t_i)\|^2}{\|\delta f\|^2} = \sum_{n,l \in Z} \frac{|(\delta d)_{m,n,l}^{\alpha\beta}(t_i)|^2}{\|\delta f\|^2}, \tag{23}$$

where $\{(\delta d)_{m,n,l}^{\alpha\beta}\}$ are the wavelet decomposition coefficients of δf,

$$\|\delta f\|^2 = \sum_{m \in Z} \sideset{}{'}\sum_{\alpha,\beta \in \{L,H\}} \|(\delta f)_m^{\alpha\beta}\|^2, \tag{24}$$

and the summation $\sum_{\alpha,\beta \in \{L,H\}}'$ also excludes $\alpha = \beta = L$. Similarly, the above WMA projects the dynamical change into different frequency sub-bands. This enable us to observe the dynamical change at different scales. Therefore, MAC characterizes the spatial complexity of the rate of change of the spatiotemporal system at each time. For simplicity, we also denote the MAC indices by abbreviation $\text{hh}_m(t_i) = \rho_{\text{MAC}}^{\text{HH}m}(t_i)$.

3. Numerical experiments

In this section, we examine the validity and demonstrate the utility of the proposed wavelet method for spatiotemporal pattern characterization. The Cahn–Hilliard (CH) equation in a circular domain is used as a model to create spatiotemporal patterns. Theoretical analysis of experiments is presented in three subsections.

3.1. The mathematical model and numerical solution

The CH equation [55,56] is a well known phenomenological model describing the dynamics of phase separation and pattern formation in many physical systems, such as alloys, polymer blends and other binary mixtures. In its dimensionless form, the CH equation is given by

$$\frac{\partial \Psi}{\partial t} = \frac{1}{2} \nabla^2 (-\nabla^2 \Psi - \Psi + \Psi^3), \tag{25}$$

where the scalar field, $\Psi(\mathbf{r}, t)$ $(-1 \leq \Psi(\mathbf{r}, t) \leq 1)$, is a conserved order parameter. In the present work, we consider the CH equation in a circular domain. Such a geometry and the nonlinear nature of the governing equation give rise to fascinating spatiotemporal patterns [34].

It turns out that this numerical integration is very technically demanding [34]. A wavelet-based discrete singular convolution (DSC) algorithm [57] is utilized to overcome the numerical difficulties. The standard implicit Crank–Nicolson scheme is used for the temporal discretization. The nonlinear terms are linearized by using a Newton-like technique. Coupled collocation equations are solved at each time step by a standard direct solver. For all simulations, we choose 32 and 64 grid points in the r and θ directions, respectively. The DSC bandwidth parameters and regularization parameters [57] are set to 30 and $\sigma_q/\Delta_q = 3.8$ $(q = r, \theta)$ in both directions.

The radius (R) of the circular domain is used as a control parameter to regulate the pattern morphology and its temporal evolution. A given random field, generated by small amplitude noise (about 10^{-2}) inside the circular domain, is used as the initial values for all computations. Motivated by the underlying physics, we impose the Dirichlet boundary condition ($\Psi(\mathbf{r}, t) = 0$) at the edge of the circular domain.

Spatiotemporal patterns are generated by integrating Eq. (25) at a set of selected control parameters, ranging from $R = 1$ to 14. At each given radius, we integrated Eq. (25) up to 2000 time units, and some particular runs are integrated up to 2600 time units to obtain certain ordered state patterns [34]. Fig. 3 shows the mesh and contour plots of some typical ordered state patterns which are observed from the long time propagation of the initial random
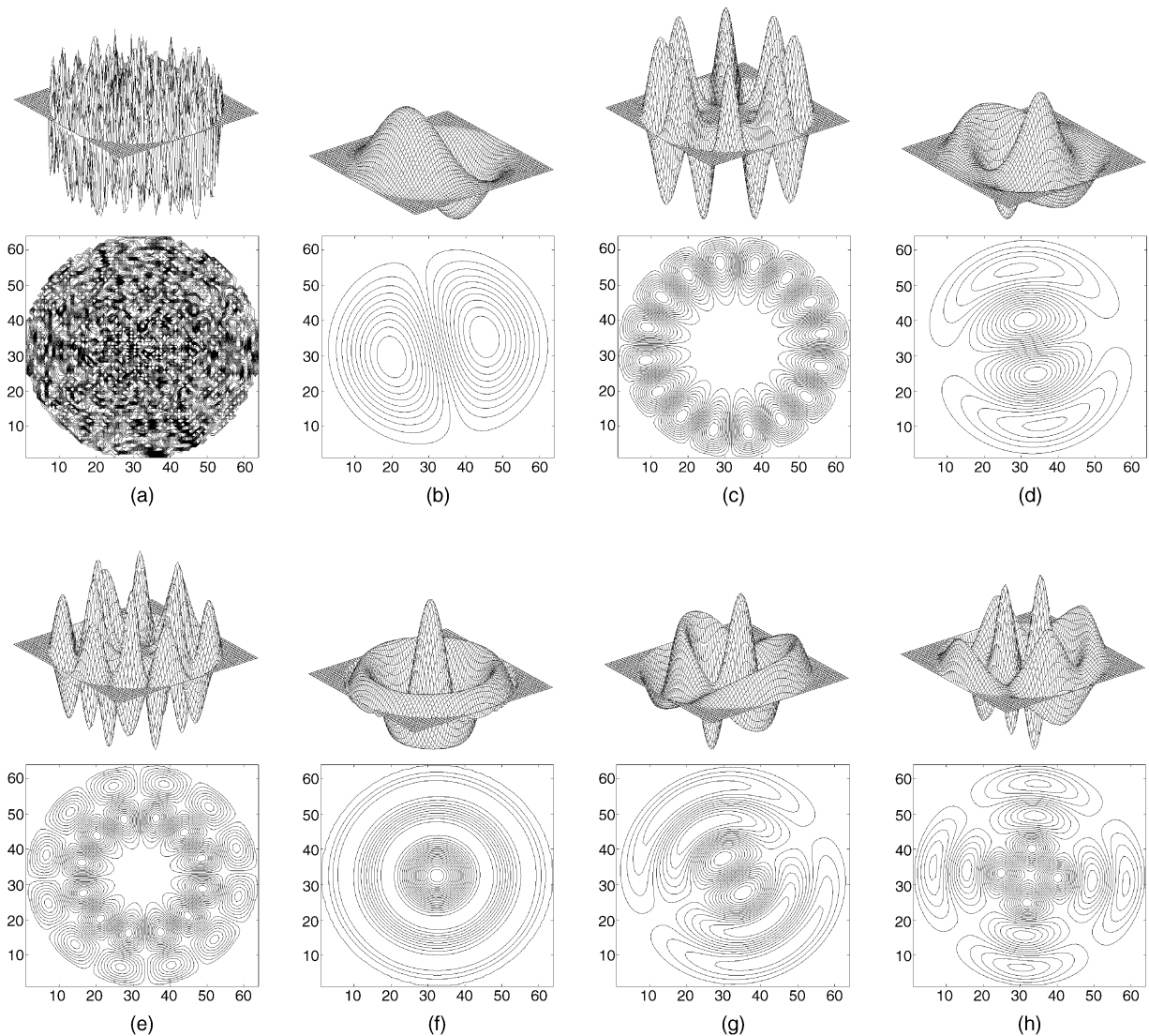
Fig. 3. (a) The initial values; (b)–(h) mesh and contour plots of typical ordered state patterns classified by their corresponding principal Fourier–Bessel modes (the most energetic modes) $[n, m]$. (b) $[1, 1]$, $R = 4.0$, $t = 1000$; (c) $[1, 8]$, $R = 11.375$, $t = 1000$; (d) $[2, 1]$, $R = 6.5$, $t = 910$; (e) $[2, 6]$, $R = 12.5$, $t = 1000$; (f) $[3, 0]$, $R = 8.25$, $t = 760$; (g) $[3, 1]$, $R = 9.75$, $t = 740$; (h) $[3, 2]$, $R = 10.875$, $t = 1000$.

Table 2

A comparison of control parameters R used for attaining ordered state patterns and the corresponding non-trivial roots, $\rho_{m,n}$, of the Bessel function

m	$n = 1$		$n = 2$		$n = 3$		$n = 4$	
	R	$\rho_{1,m}$	R	$\rho_{2,m}$	R	$\rho_{3,m}$	R	$\rho_{4,m}$
0	–	–	5.5	5.520	8.25	8.654	11.0	11.792
1	4.0	3.832	6.5	7.016	9.75	10.173	–	–
2	5.0	5.136	8.0	8.417	10.875	11.620	–	–
3	6.0	6.380	9.25	9.761	12.0	13.015	–	–
4	7.5	7.588	10.5	11.065	–	–	–	–
5	8.5	8.771	11.5	12.339	–	–	–	–
6	9.375	9.936	12.5	13.589	–	–	–	–
7	10.0	11.086	–	–	–	–	–	–
8	11.375	12.225	–	–	–	–	–	–

values. The basic morphology of these patterns is that of concentric rings of cells. Each cell is actually a single-phase domain of either component A or component B, which is formed through microphase separations. Notably, there exist interesting symmetric aspects in the observed ordered state patterns. Traditionally, the circular spatiotemporal patterns can be analyzed and characterized by Fourier–Bessel decomposition. Fourier–Bessel decomposition reveals that the ordered state patterns can be expressed as linear combinations of Fourier–Bessel functions [34]. For small control parameter, usually there exists a principal Fourier–Bessel mode which contributes most significantly to the ordered state pattern and predominantly determines the morphology of the pattern. This principal Fourier–Bessel mode is excited when the control parameter R is close to the corresponding theoretical roots of Bessel functions. In Fig. 3, we only selectively illustrate a few observed patterns. The control parameters corresponding to all the four complete series of ordered state patterns are listed in Table 2. Moreover, morphological evolution of the spatiotemporal patterns gives rise to diverse dynamical behaviors, including steady states, uniform oscillations, modulated oscillations and chaotic dynamics [33].

3.2. Multiscale pattern analysis

To analyze the ordered state patterns, three-scale WMA as illustrated in Fig. 2(a) is performed. Daubechies-8 wavelets [52] are used for all computations. Fig. 4(b)–(e) depicts the contour plots of the three-scale wavelet decomposition amplitudes of the ordered state patterns shown in Fig. 3(b)–(e). In order to achieve an enhanced visualization effect, results plotted in Fig. 4 are obtained by the wavelet transform of the square of patterns f^2. Since Fig. 3(b) contains a relatively smooth pattern, its three-scale wavelet transform, Fig. 4(b), has non-zero components concentrating in a few low frequency sub-bands, such as LL_1, LH_1 and HL_1. The smoothest sub-band, LL_1, has most of the "density". The pattern in Fig. 3(c) contains more high frequency components than that in Fig. 3(b). Therefore, its wavelet transform, Fig. 4(c), has non-zero components in all the 10 sub-bands, most notably, in sub-bands LH_2 and HL_2. Similarly, Fig. 4(d) indicates that the pattern in Fig. 3(d) has little high frequency wavelet filter response, whereas the pattern in Fig. 3(e) displays much dramatical spatial variance as can be noted from its wavelet decomposition, Fig. 4(e). Fig. 4(a) depicts the wavelet sub-band filter responses of the initial Gaussian random noise. Unlike the ordered state patterns, the random noise has intensive scattered filter responses over all the frequency sub-bands, particularly in the HH_3 sub-band. In Table 3, the MAD indices are listed for a comparison for the initial values of Fig. 3(a) and the typical ordered state patterns shown in Fig. 3(b)–(e). Ordered state patterns, Fig. 3(b) and (d), have relatively large MAD indices in the low frequency sub-bands (LH_1, HL_1 and LL_1). These two patterns have relatively large single-phase domains. In contrast, ordered state patterns Fig. 3(c) and (e) have

(a)

(b)
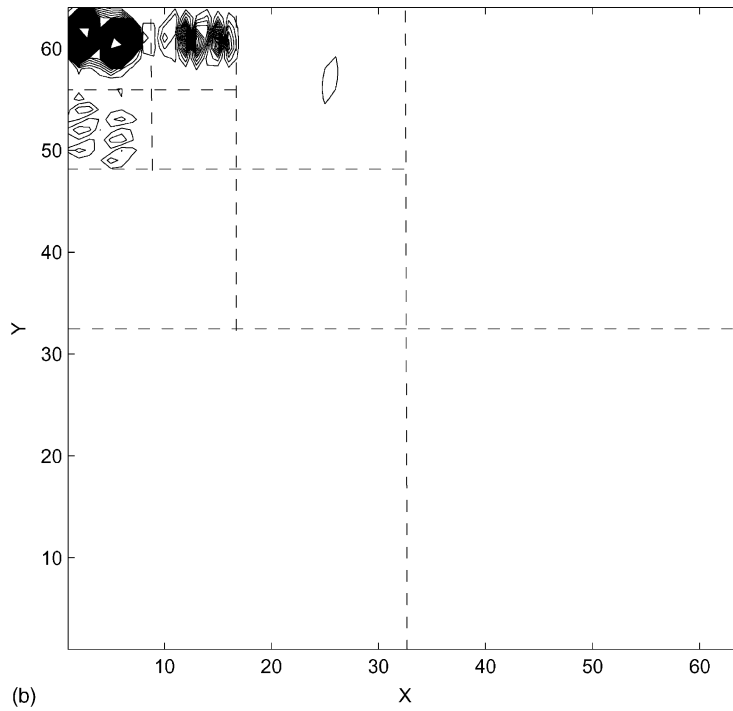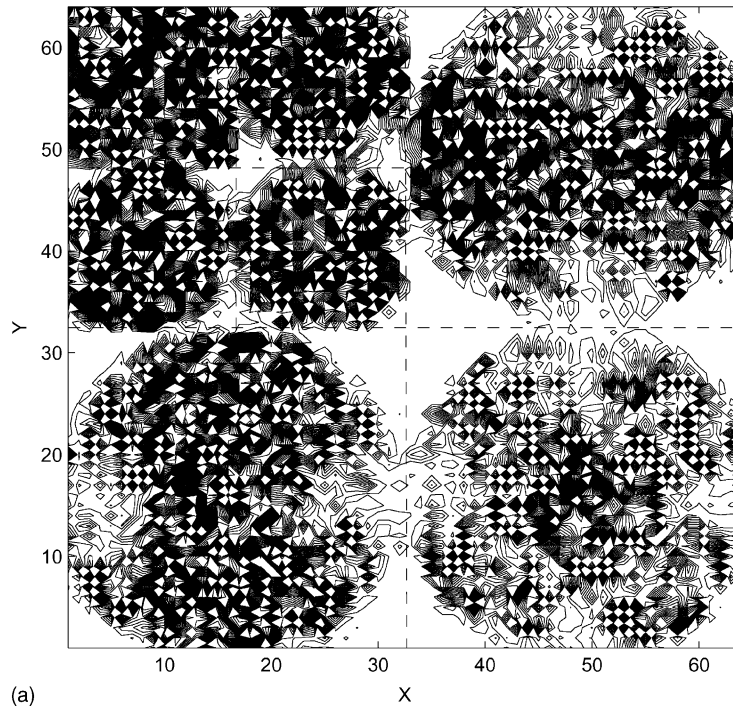
Fig. 4. (a)–(e) Contour plots of the wavelet decomposition amplitudes of the initial condition (Fig. 3(a)) and the ordered state patterns shown in Fig. 3(b)–(e).

(c)

(d)

Fig. 4. (*Continued*).

(e)
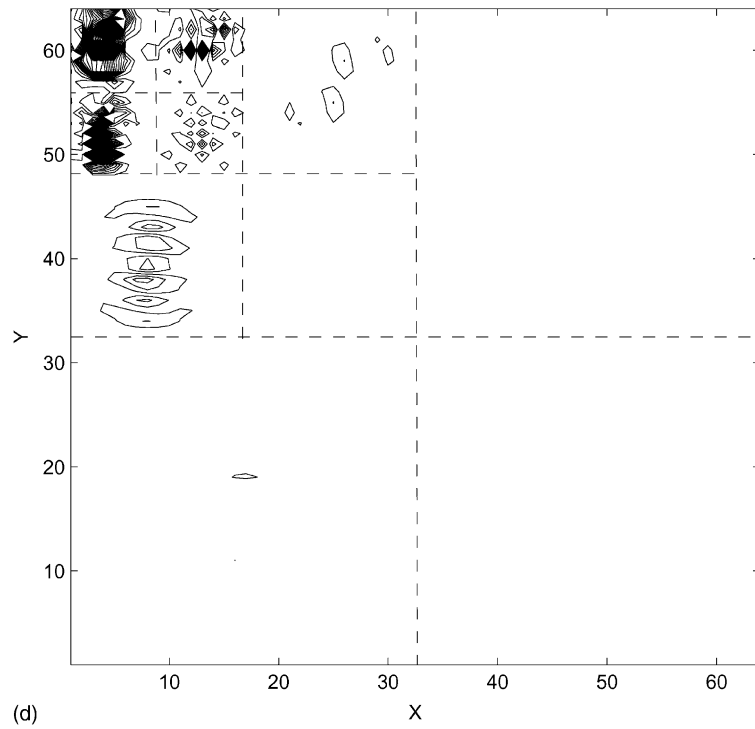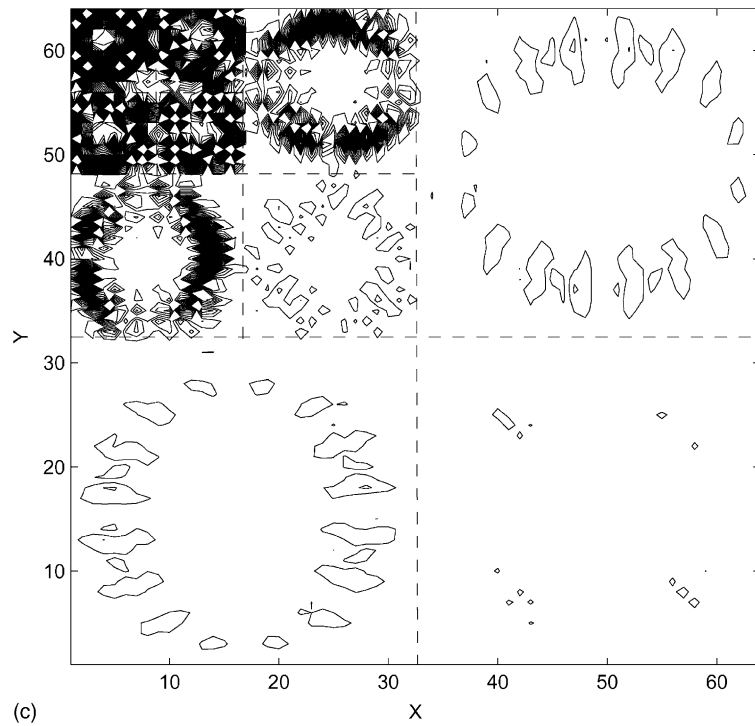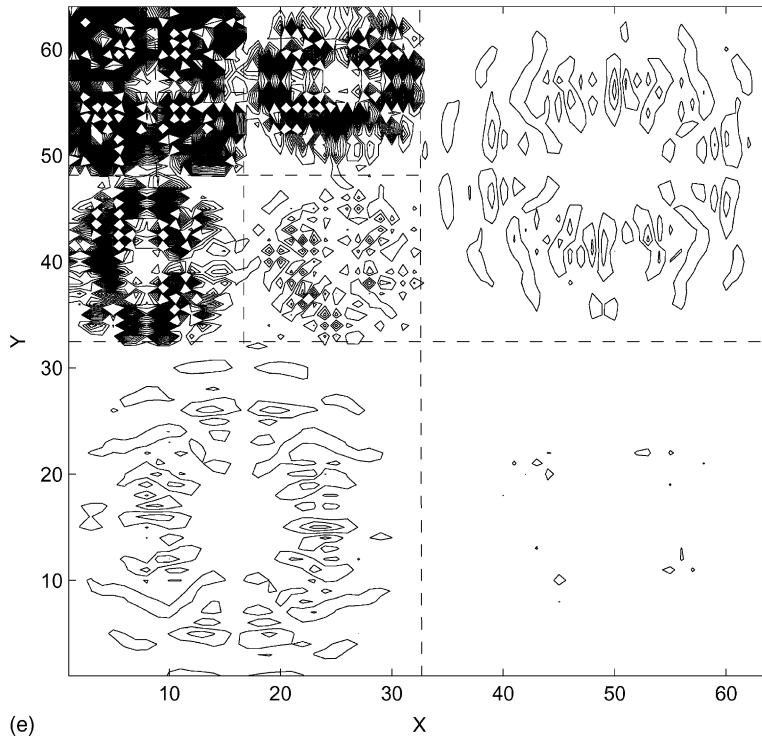
Fig. 4. (*Continued*).

relatively large MAD indices in the high frequency sub-bands (LH_3, HL_3 and HH_3). Their morphology is more complicated than that of Fig. 3(b) and (d). Nevertheless, a common feature for the MAD indices of ordered state patterns is that the ratio of LL_1/HH_3 is much larger than one. Such a ratio reflects the spatial coherence order in the pattern. In general, the larger ratio, the higher the coherence order is in the pattern. The values of LL_1/HH_3 ratio for Fig. 3(a)–(e) are 0.278, 0.305×10^7, 0.262×10^5, 0.708×10^6, 0.116×10^5, respectively. Clearly, the initial Gaussian random noise has a very small ratio (0.278) and consequently, a very low coherence order. The pattern in Fig. 3(b) has the largest single-phase domains and the highest coherence order as indicated by the largest ratio

Table 3
The MAD indices of the initial values and some typical ordered state patterns

MAD index	Fig. 3(a)	Fig. 3(b)	Fig. 3(c)	Fig. 3(d)	Fig. 3(e)
HH_3	$0.930E-1$	$0.327E-6$	$0.229E-4$	$0.137E-5$	$0.461E-4$
LH_3	0.217	$0.303E-5$	$0.136E-3$	$0.181E-5$	$0.238E-3$
HL_3	0.218	$0.577E-6$	$0.136E-3$	$0.178E-4$	$0.239E-3$
HH_2	$0.932E-1$	$0.908E-6$	$0.747E-4$	$0.444E-5$	$0.248E-3$
LH_2	0.133	$0.283E-4$	$0.479E-2$	$0.566E-4$	$0.943E-2$
HL_2	0.115	$0.526E-5$	$0.479E-2$	$0.391E-3$	$0.946E-2$
HH_1	$0.396E-1$	$0.616E-5$	$0.532E-2$	$0.185E-3$	$0.101E-1$
LH_1	$0.317E-1$	$0.159E-2$	0.192	$0.412E-2$	0.217
HL_1	$0.337E-1$	$0.314E-3$	0.192	$0.255E-1$	0.217
LL_1	$0.258E-1$	0.998	0.600	0.970	0.536

of 0.305×10^7. Therefore, the ratio of LL_1/HH_3 can be quantitatively used to measure the formation of spatially coherent structures in the present pattern-forming system.

The mechanism of the formation of ordered state patterns can be regarded as the results of a frequency competition process, which is driven by the nonlinear force in the CH equation. By competition, only a few spatial frequencies can survive to dominate the system. Physically, this corresponds to the formation of the spatially coherent structures. If the "energy" of the system is measured by $(1/2) \int |\nabla \Psi|^2 \, d\mathbf{x}$, it is easy to prove that the formation of ordered state patterns is a nonlinear dispersive process. This energy loss can be visualized directly from wavelet sub-band filter responses. Note that Eq. (25) itself says nothing about energy conservation. Physically, the reduction in total energy leads to stable states. Moreover, the formation of large smooth domain in wavelet sub-band LL_1 indicates the mass transfer in the pattern formation process.

It should be noted that patterns discussed in this subsection are ordered state patterns which are obtained from the long time integration of the CH equation. Since the system under study is in the "small" and "moderately large" regime, the characterization length of the ordered state patterns is comparable to the system size. Our wavelet analysis indicates that ordered state patterns can be effectively analyzed by wavelet sub-band energy. In other words, each wavelet quadratic mirror filer response can be used as a quantitative monitoring index for mass transfer and energy dispersion. Quantitative wavelet characterization of the dynamics of the spatiotemporal patterns is presented in the next section.

3.3. Characterization of morphological pattern evolution

In this section, the wavelet multiresolution indices, the MAD and MAC are used to characterize the morphological evolution of the spatiotemporal patterns. We first carry out the MAD index analysis to the spatiotemporal patterns. This is done by computing the MAD index at each time step. The dynamical information is revealed in the time series of the MAD index which is constructed from the solution of the CH equation. The MAC analysis is performed for a few selected cases. By using the time series of MAD and MAC as indices, a wide variety of morphological pattern evolutions are characterized.

3.3.1. MAD Characterization

Steady state. A typical example of a steady state is shown in Fig. 5. The temporal evolutions of three MAD indices $HH_3(t_i)$, $HH_2(t_i)$ and $HH_1(t_i)$ are plotted. Obviously, the system stabilizes at the steady state only after a short transient period. During this transient period, the coherence order is very low and the ordered state has not been established. The morphology of the system is characterized by the random arrangement of the small single-phase domains. Physically, this corresponds to the mass transfer and energy dispersion during the phase separation and pattern formation in the non-equilibrium systems.
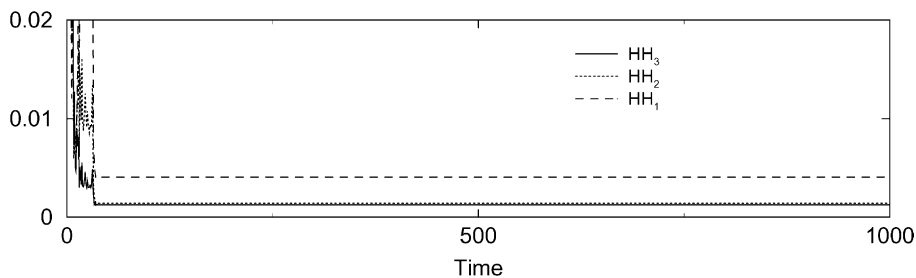
Fig. 5. The MAD indices $HH_m(t_i)$ ($m = 1, 2, 3$), $R = 5.5$.
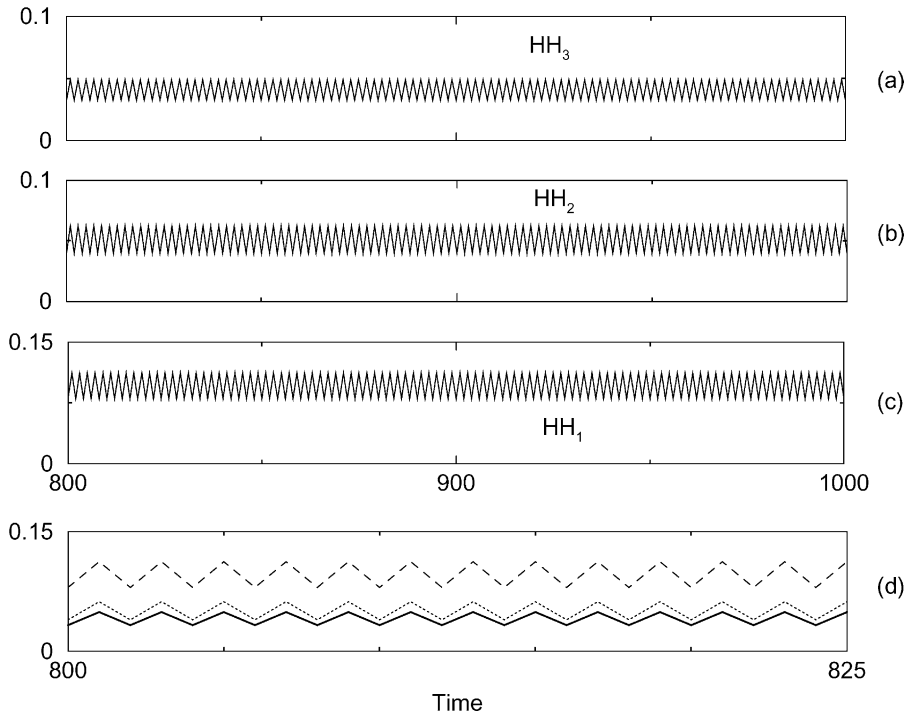
Fig. 6. (a)–(c) The MAD indices $HH_m(t_i)$ ($m = 1, 2, 3$); (d) solid: $HH_3(t_i)$; dotted: $HH_2(t_i)$; dashed: $HH_1(t_i)$. $R = 4.0$.

Uniform oscillation. The time evolution of principal Fourier–Bessel modes often oscillates periodically in the present system. The observed periodic oscillations can be further divided into two types. One is the uniform oscillation and the other is the modulated oscillation.

Fig. 6 demonstrates a typical example where the MAD indices undergo a uniform oscillation. It is found that all the three MAD indices $HH_m(t_i)$ ($m = 1, 2, 3$) are frequency-locked and they change from the positive maximal amplitude to the negative minimal amplitude alternatively. This implies that the morphological pattern evolution in this example is a period-2 orbit and the spatial patterns have certain self-similar properties. One of involved ordered state patterns is shown in Fig. 3(b).

Modulated oscillation. Figs. 7 and 8 depict two examples of the modulated oscillations. It is found that the morphological pattern evolutions are period-3 orbit and period-7 orbit, respectively. Usually, there are several transient states inside one modulated period. Although inside one modulated period, three MAD indices are not totally frequency-locked as in the uniform oscillation described in the last example, they can correctly characterize the global trend of the morphological pattern evolution. Therefore, the MAD indices at any of the three scales can be used to characterize the dynamics of the spatiotemporal patterns.

Fig. 9(a) and (b) presents two more examples of the modulated morphological evolution. These two typical examples have very long modulated period orbits. In Fig. 9(a), the orbit of the MAD indices is period 24, while in Fig. 9(b) the orbit of the MAD indices is period 50. In both cases, the evolutions inside one period are strongly modulated due to the complicated competition inside the system.

The morphological pattern evolution at $R = 12.5$ is very special, as demonstrated by the MAD indices in Fig. 10. At the beginning, the system goes into the steady state after a short period of transient states. Then after a period
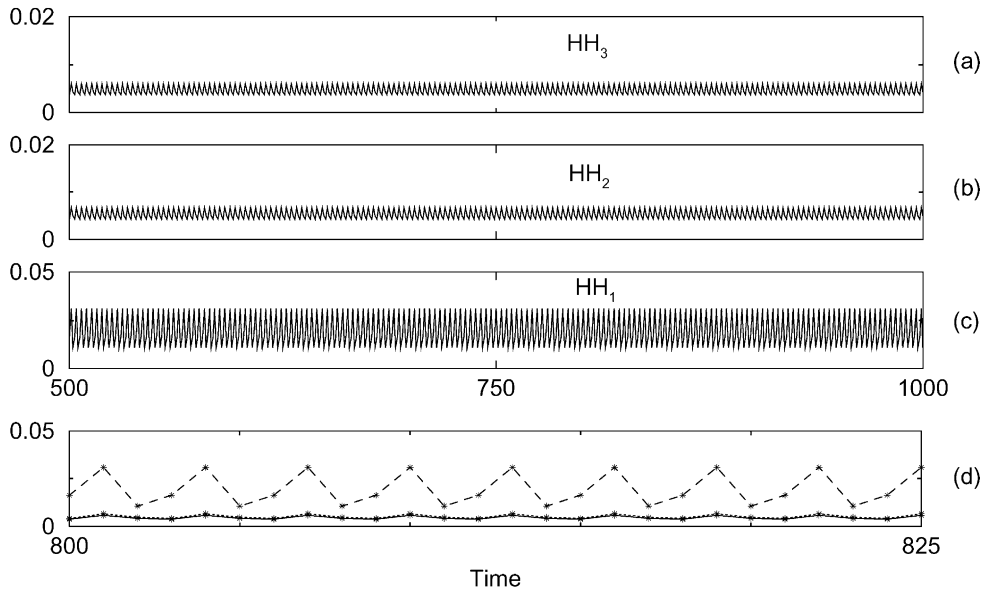
Fig. 7. (a)–(c) The MAD indices $HH_m(t_i)$ ($m = 1, 2, 3$); (d) solid: $HH_3(t_i)$; dotted: $HH_2(t_i)$; dashed: $HH_1(t_i)$. $R = 7.0$.
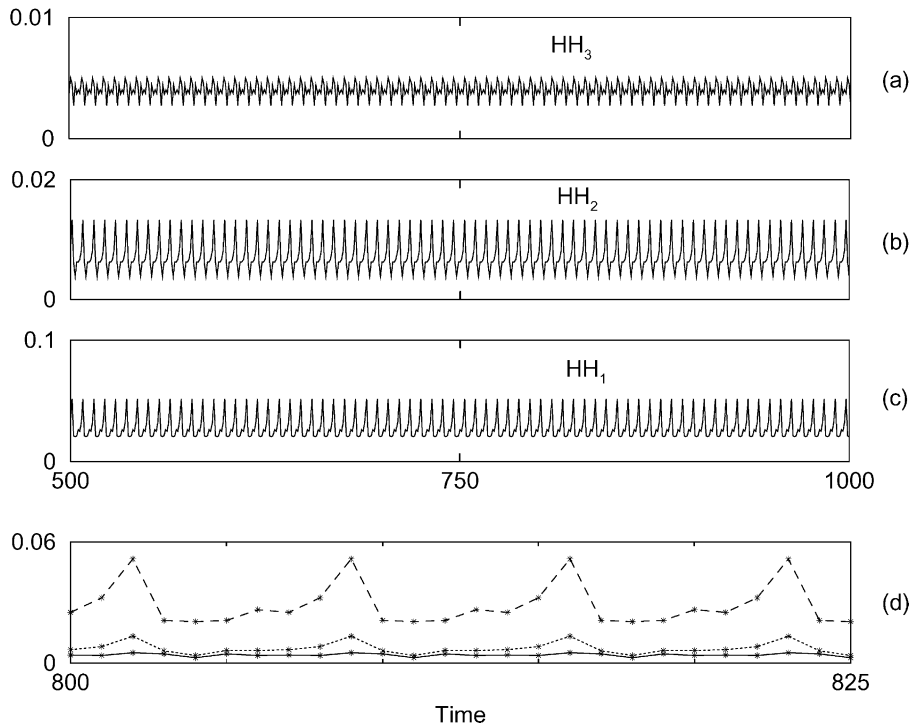
Fig. 8. (a)–(c) The MAD indices $HH_m(t_i)$ ($m = 1, 2, 3$); (d) solid: $HH_3(t_i)$; dotted: $HH_2(t_i)$; dashed: $HH_1(t_i)$. $R = 9.25$.
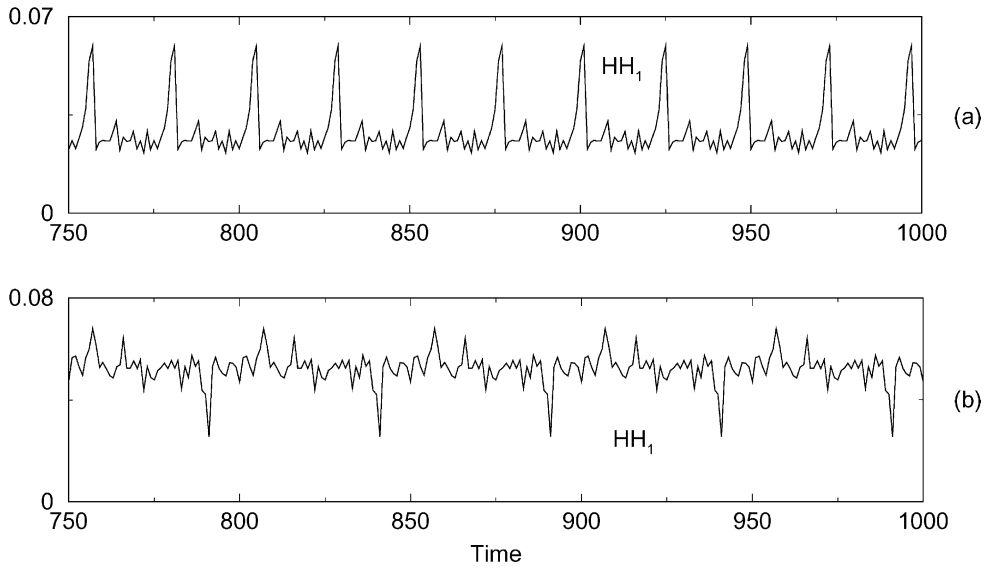
Fig. 9. The MAD indices $HH_1(t_i)$: (a) $R = 9.75$, (b) $R = 12.0$.

of evolution of the steady state, the system converts to the modulated oscillation. A typical ordered state pattern is depicted in Fig. 3(e).

Chaotic oscillation. Besides the periodic morphological evolutions, the chaotic morphological evolutions also occur frequently in the present system. In Figs. 11 and 12, we demonstrate the chaotic morphological evolution of patterns characterized by the disordered evolution of the MAD indices. A typical ordered state pattern corresponding
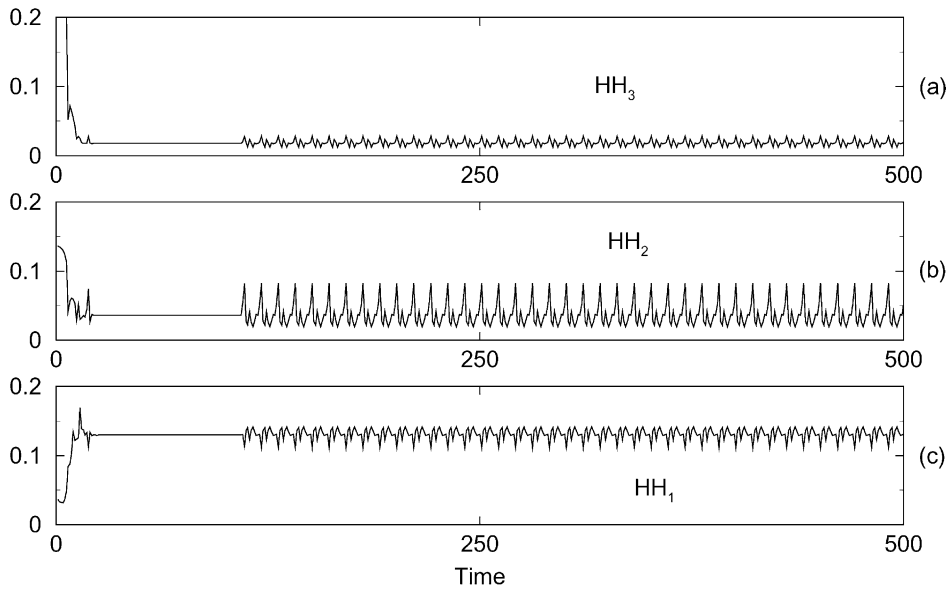
Fig. 10. The MAD indices $HH_m(t_i)$ ($m = 1, 2, 3$), $R = 12.5$.
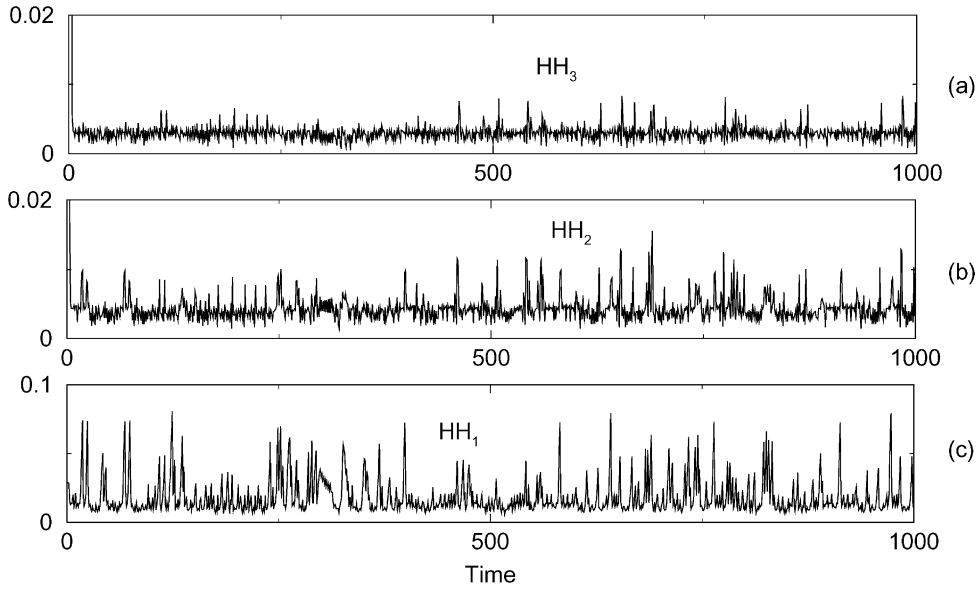
Fig. 11. The MAD indices $HH_m(t_i)$ ($m = 1, 2, 3$), $R = 6.5$.

to Fig. 11 is depicted in Fig. 3(d). In Fig. 13, we plotted the morphological evolution of the "patterns" at successive six time steps corresponding to Fig. 12. Fourier–Bessel analysis shows that these "patterns" are actually the mixture of many Fourier–Bessel modes [33]. From Fig. 13, we can see that the spatially coherent structures are partially destroyed due to the modal competition. Nevertheless, there still exist many single-phase domains. In the literature, this phenomenon is known as "weak turbulence". For chaotic evolutions of spatiotemporal patterns, it is found that
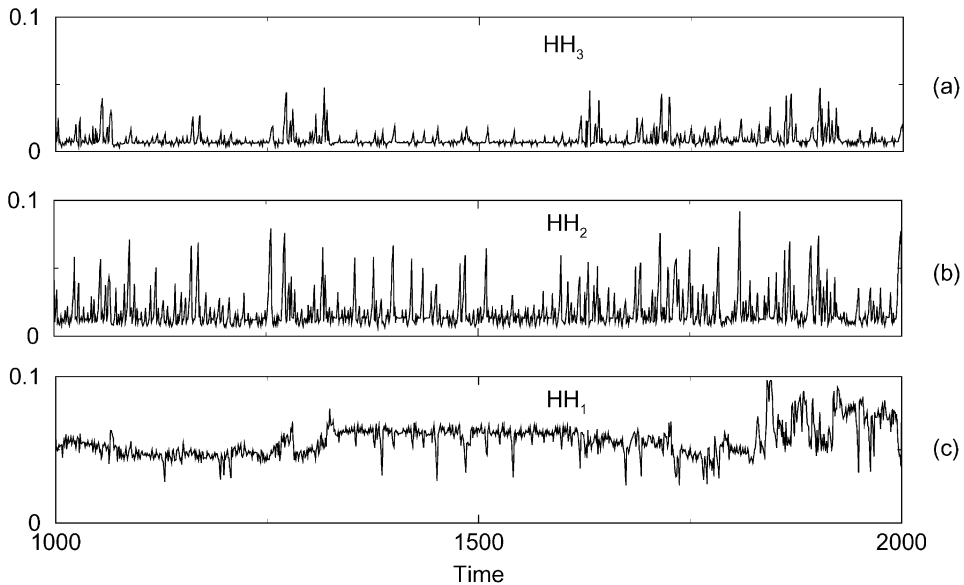
Fig. 12. The MAD indices $HH_m(t_i)$ ($m = 1, 2, 3$), $R = 13.5$.
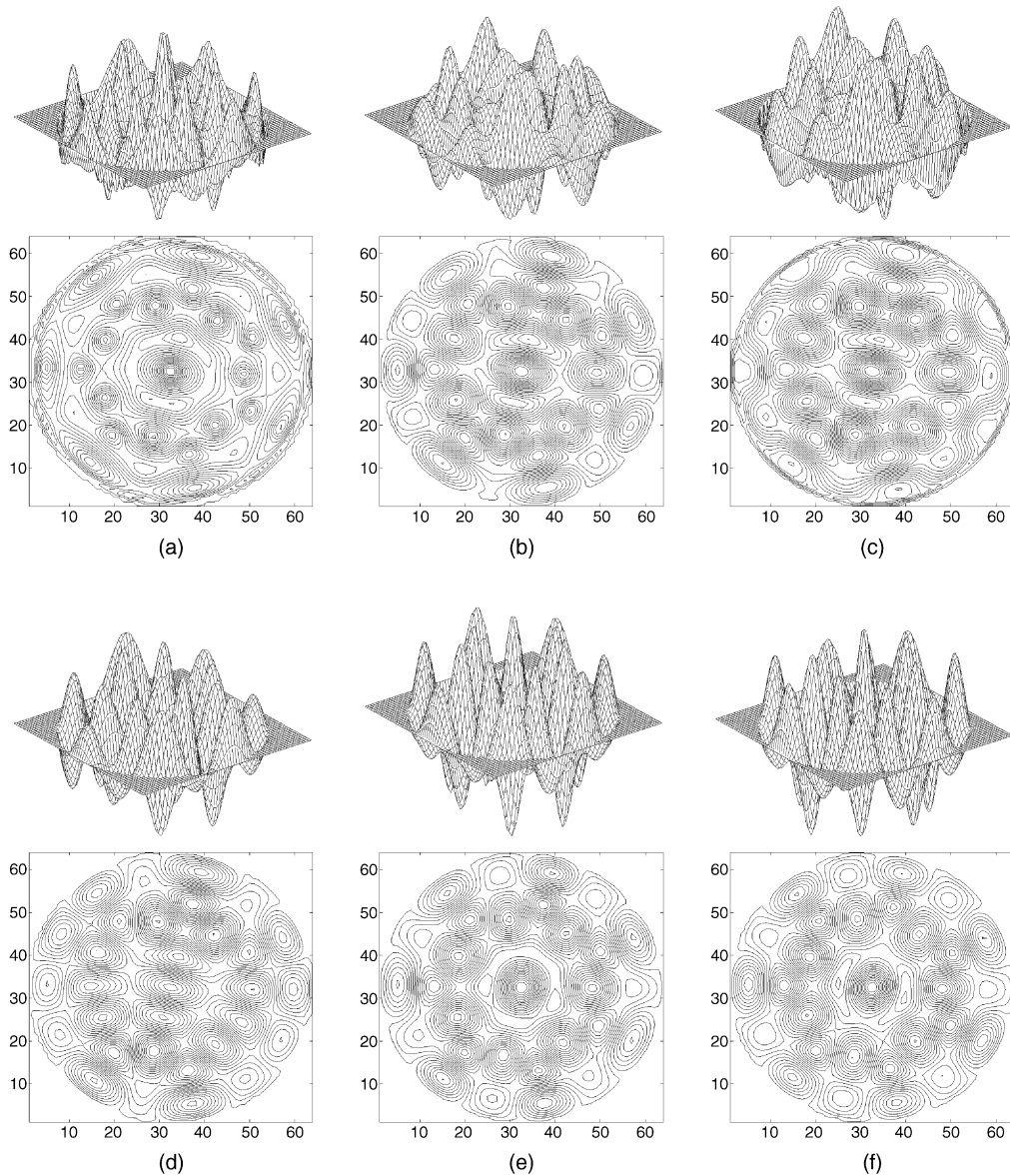
Fig. 13. The six successive "patterns" from $t = 814$ to 819, $R = 13.5$.

the MAD indices at different scales are different. It is noted that the scalings of the vertical axis in Figs. 11 and 12 are different. There is more "density" distributed in the lower frequency band in Fig. 12. In general, the MAD indices of $HH_1(t_i)$ are larger than those of $HH_3(t_i)$ and $HH_2(t_i)$.

Intermittency is a typical kind of chaotic motion. Its evolution is observed in the present study. Two typical examples are shown in Figs. 14 and 15. In these cases, the irregular oscillation and the regular oscillation dominate the evolution alternatively for different time intervals. In Fig. 14, three MAD indices all demonstrate the same intermittent evolution. Fig. 15 depicts another case of intermittency dynamics, which is similar to that shown in
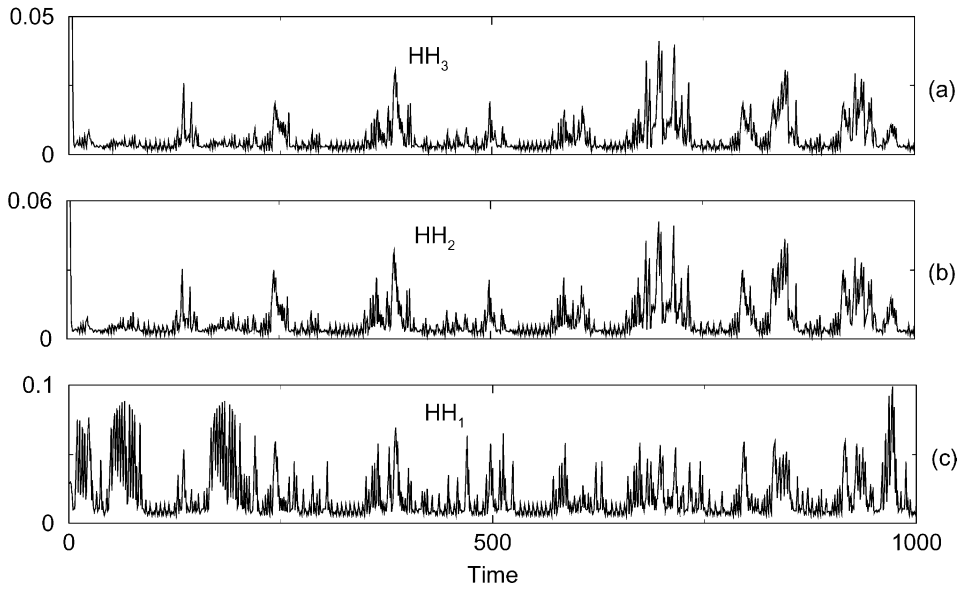
Fig. 14. The MAD indices $HH_m(t_i)$ ($m = 1, 2, 3$), $R = 6.0$.

Fig. 10. For the first 800 time steps, the system undergoes intermittent oscillation. Subsequently, the system converts to modulated oscillations.

For periodic oscillations, all the MAD indices can characterize the same dynamics. In such cases, actually only one index is sufficient for the characterization of the morphological pattern evolution. On the other hand, for chaotic oscillations, the indices at different scales can be very different. In this case, we conjecture that among all the MAD
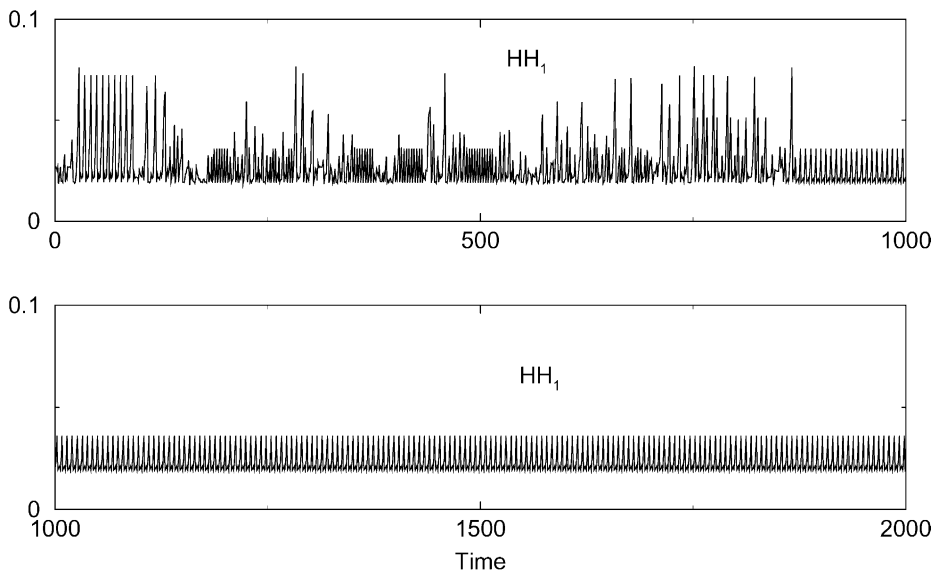
Fig. 15. The MAD indices $HH_1(t_i)$, $R = 9.375$.

indices, as long as there exists one index series whose dynamics is chaotic (characterized by positive Lyapunov exponent), the morphological evolution of the spatiotemporal patterns can be regarded as chaotic. This conjecture has been confirmed by estimation of the Lyapunov exponents of the MAD indices for chaotic morphological pattern evolutions. For instance, although the three Lyapunov exponents of $HH_3(t)$, $HH_2(t)$ and $HH_1(t)$ shown in Fig. 14 are not the same, they are all positive. This implies that the MAD indices can correctly represent the global trend of the morphological evolution of the spatiotemporal patterns.
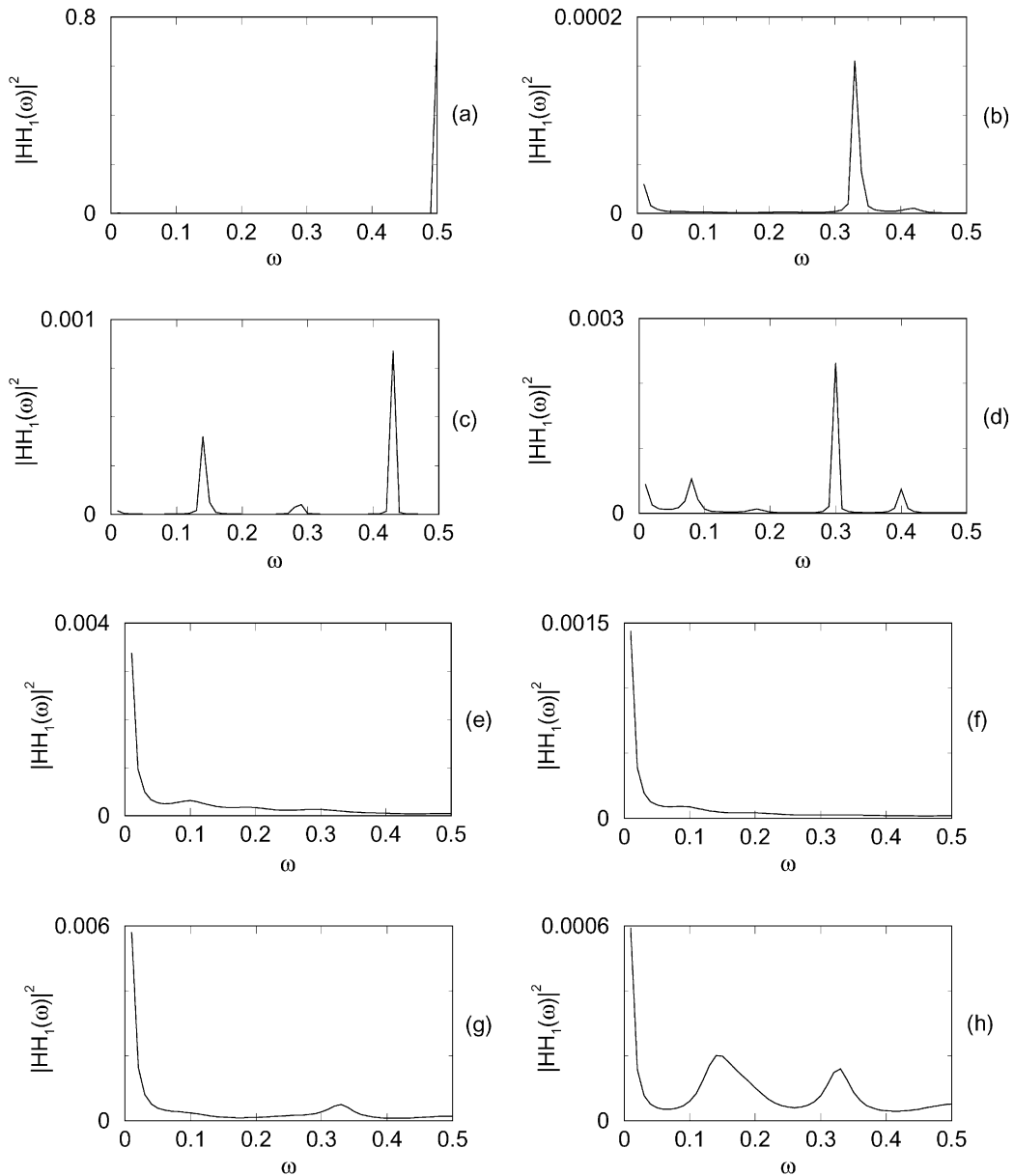
Fig. 16. Power spectra of the MAD indices $HH_1(t_i)$: (a) $R = 4.0$; (b) $R = 7.0$; (c) $R = 9.25$; (d) $R = 12.5$; (e) $R = 6.5$; (f) $R = 13.5$; (g) $R = 6.0$; (h) $R = 9.375$. To minimize the influence of the initial condition to the dynamics, the data of the first 500 time steps are excluded.
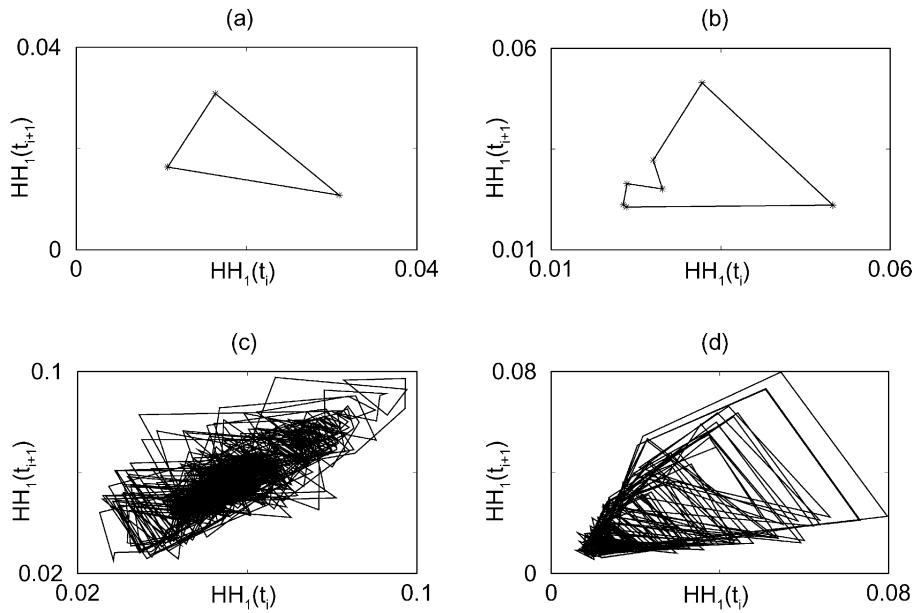
Fig. 17. Phase plane plots of $HH_1(t_i)$ vs $HH_1(t_{i+1})$: (a) $R = 7.0$; (b) $R = 9.25$; (c) $R = 13.5$; (d) $R = 6.5$. The data of the first 500 time steps are excluded.

The dynamics of the MAD indices can be further analyzed and confirmed by their power spectra and phase plane plots. Fig. 16 shows some of the power spectra and Fig. 17 depicts some typical phase plane plots of some typical dynamics of the spatiotemporal patterns discussed above. The results are consistent with our previous Fourier–Bessel analysis [33].
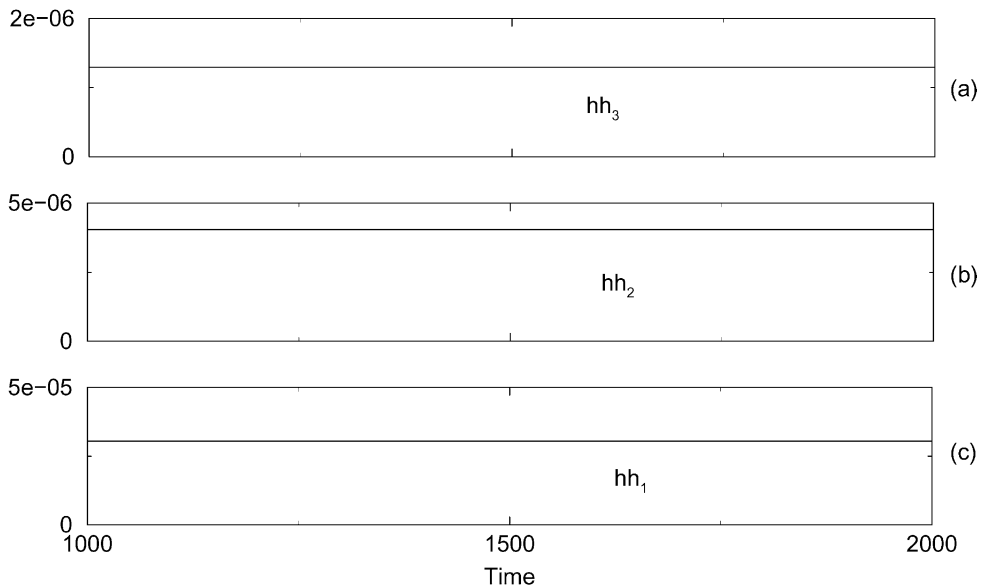
Fig. 18. The MAC indices $hh_m(t_i)$ ($m = 1, 2, 3$), $R = 4.0$.
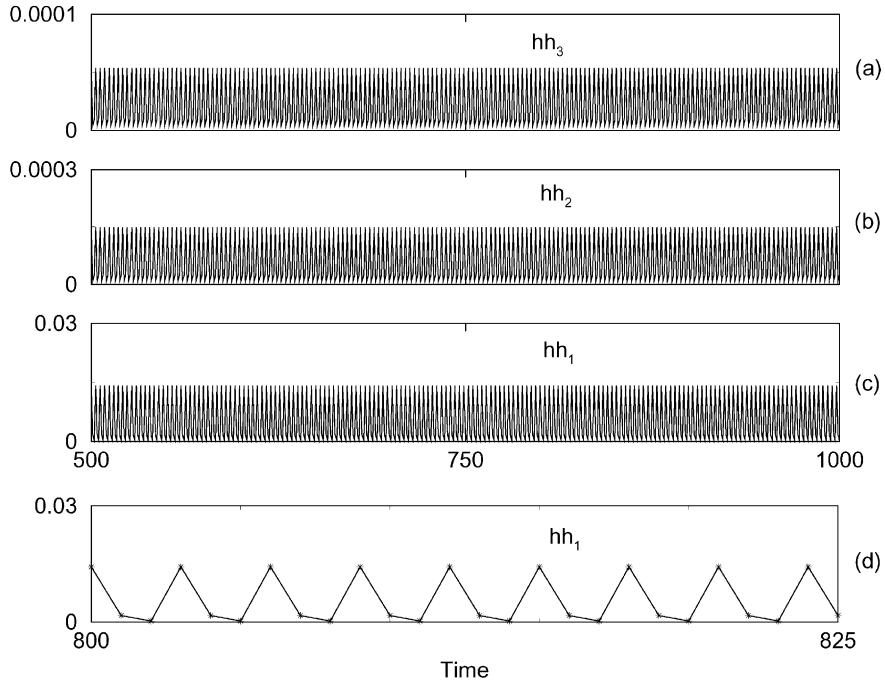
Fig. 19. (a)–(c) The MAC indices $hh_m(t_i)$ ($m = 1, 2, 3$); (d) enlarged plot of $hh_1(t_i)$. $R = 7.0$.
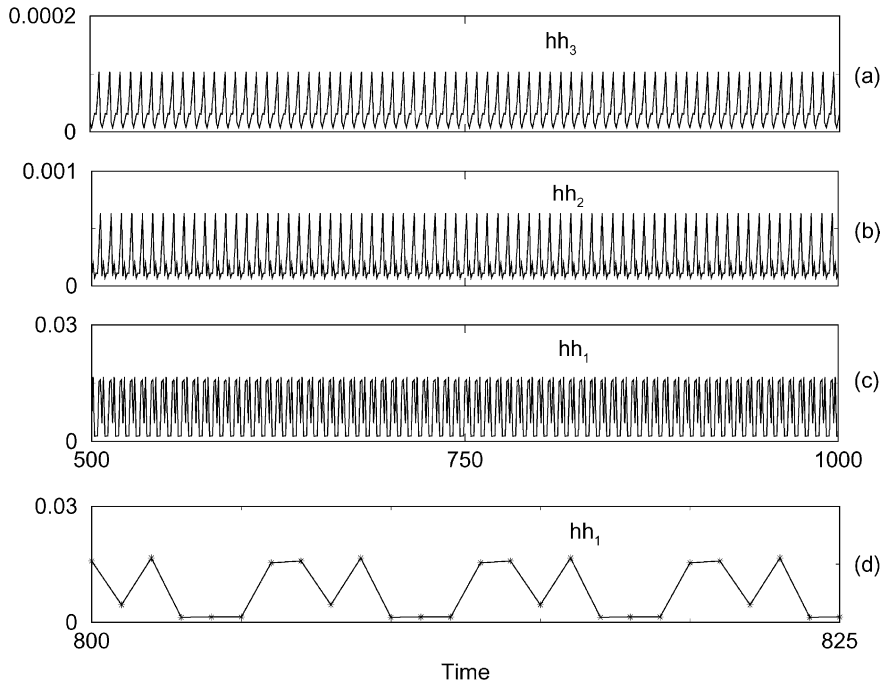
Fig. 20. (a)–(c) The MAC indices $hh_m(t_i)$ ($m = 1, 2, 3$); (d) enlarged plot of $hh_1(t_i)$. $R = 9.25$.
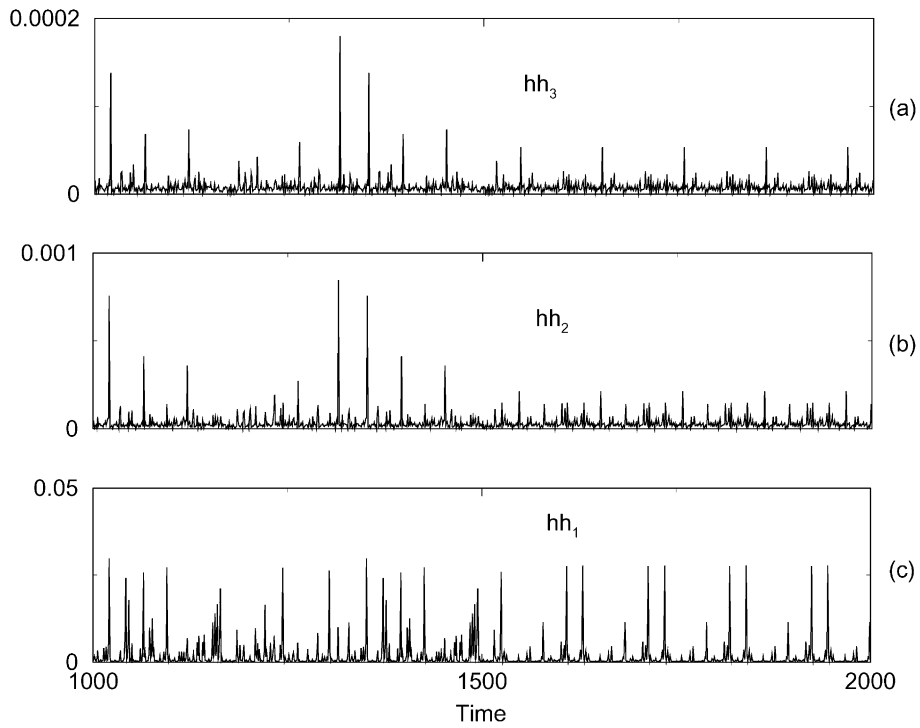
Fig. 21. The MAC indices $hh_m(t_i)$ $(m = 1, 2, 3)$, $R = 6.5$.
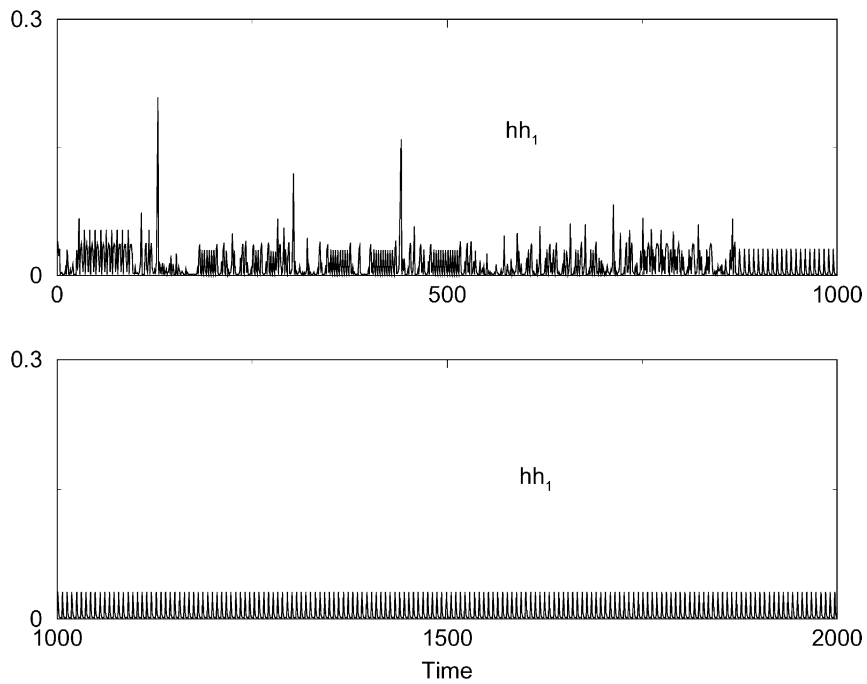
Fig. 22. The MAC indices $hh_1(t_i)$, $R = 9.375$.
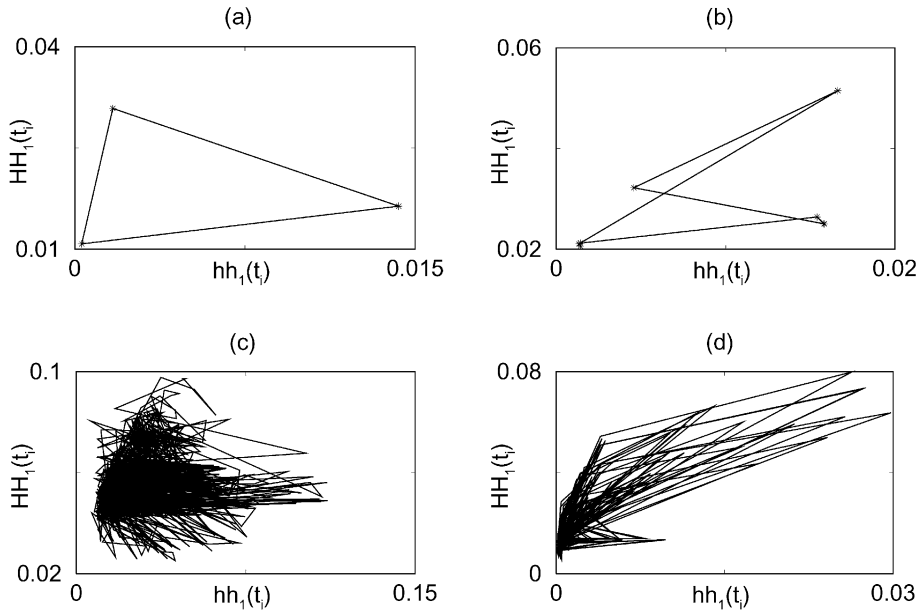
Fig. 23. "Phase plane" plots of $HH_1(t_i)$ vs $hh_1(t_i)$: (a) $R = 7.0$; (b) $R = 9.25$; (c) $R = 13.5$; (d) $R = 6.5$. The data of the first 500 time steps are excluded.

3.3.2. MAC characterization

Complementary to the MAD indices $HH_m(t_i)$ ($m = 1, 2, 3$), the MAC indices $hh_m(t_i)$ ($m = 1, 2, 3$) can provide another faithful representation of the morphological evolution of the spatiotemporal patterns. Figs. 18–22 give some examples. The MAC time series in Fig. 18 corresponds to the MAD indices of Fig. 6. The underlying dynamics is a uniform oscillation. Since the MAC indices characterize the spatial complexity of the change, uniformly oscillatory MAD indices in Fig. 6 reduce to steady MAC indices in Fig. 18. Figs. 19 and 20 present two other examples of MAC indices corresponding to those in Figs. 7 and 8, respectively. It is found that the MAC indices exhibit modulated oscillations which are similar to those found in the MAD indices. Moreover, numerical experiments show that the MAC indices can provide correct dynamical information of the chaotic morphological evolutions. Figs. 21 and 22 illustrate two examples which correspond to the cases of Figs. 11 and 15, respectively. From these plots, it is seen that the dynamics characterized by the MAC indices are consistent with that characterized by the MAD indices. In Fig. 23, we depict the phase plane plots of $HH_1(t_i)$ vs $hh_1(t_i)$. They can be understood as the "reduced coordinate vs momentum" phase plots. It is found that the results in Fig. 23 is consistent with that of Fig. 17. This implies that both MAD and MAC indices can provide the same dynamical information of morphological pattern evolutions.

4. Conclusion

In this study, a wavelet-based method is proposed for both the analysis of the ordered state patterns and the characterization of the dynamics of spatiotemporal patterns. It is found that wavelet multiscale analysis can provide useful information for microphase size, modal spatial variation and formation of ordered state patterns. Wavelet decomposition also provides valuable information on mass and "energy" transport in the process of pattern formation. Based on the wavelet multiscale analysis, two wavelet indices, MAD and MAC, are introduced for the dynamical

characterization of spatiotemporal patterns. In particular, the ratio of the MAD indices between the highest and lowest scales reflects the order of coherence in a pattern. The order of coherence can in turn be used to measure the size of single-phase domains. The utility of MAD and MAC is illustrated by using numerically generated spatiotemporal patterns. It is found that a wide variety of morphological pattern evolutions, including steady state, uniform oscillation, modulated oscillation and chaotic dynamics, can be well characterized by the proposed approach. The results obtained from this method are consistent with our previous results obtained by Fourier–Bessel analysis. In contrast to existing linear decomposition methods, the use of the proposed approach does not depend on the prior knowledge about the pattern system. In addition, the proposed method is computationally efficient in the sense that it does not need to store the huge spatiotemporal data, which is necessary in the KL decomposition method. Numerical experiments indicate that the proposed method is general and efficient for the characterization of spatiotemporal patterns generated from a nonlinear dynamic system.

Acknowledgements

References

[1] C. Bowman, A.C. Newell, Natural patterns and wavelets, Rev. Mod. Phys. 70 (1998) 289.
[2] H. Kantz, T. Schreiber, Nonlinear Time Series Analysis, Cambridge University Press, Cambridge, 1997.
[3] M.C. Cross, P.C. Hohenberg, Pattern formation outside of equilibrium, Rev. Mod. Phys. 65 (1993) 854.
[4] D. Walgraef, Spatio-temporal Pattern Formation, Springer, New York, 1997.
[5] K. Kaneko, in: G. Ikegami (Ed.), Dynamical Systems and Singular Phenomena, World Scientific, Singapore, 1987.
[6] A. Torcini, A. Politi, G.P. Puccioni, G. D'Alessandro, Fractal dimension of spatially extended systems, Physica D 53 (1991) 85.
[7] N. Parekh, V.R. Kumar, B.D. Kulkarni, Analysis and characterization of complex spatio-temporal patterns in nonlinear reaction–diffusion systems, Physica A 224 (1996) 369.
[8] M. Bauer, H. Heng, W. Martienssen, Characterization of spatiotemporal chaos from time series, Phys. Rev. Lett. 71 (1993) 521.
[9] L.S. Tsimring, Nested strange attractors in spatiotemporal chaotic system, Phys. Rev. E 48 (1993) 3421.
[10] S.M. Zoldi, H.S. Greenside, Karhunen–Loéve decomposition of extensive chaos, Phys. Rev. Lett. 78 (1997) 1687.
[11] D.A. Egolf, Dynamical dimension of defects in spatiotemporal chaos, Phys. Rev. Lett. 81 (1998) 4120.
[12] L. Pezard, J. Martinerie, J. Müller-Gerking, F.J. Varela, B. Renault, Entropy quantification of human brain spatio-temporal dynamics, Physica D 96 (1996) 344.
[13] R. Carretero-González, S. Ørstavik, J. Huke, D.S. Broomhead, J. Stark, Scaling and interleaving of subsystem Lyapunov exponents for spatio-temporal systems, Chaos 9 (2) (1999) 466.
[14] S. Ciliberto, B. Nicolaenko, Estimating the number of degrees of freedom in spatially extended systems, Europhys. Lett. 14 (4) (1991) 303.
[15] A. Hutt, C. Uhl, R. Friedrich, Analysis of spatiotemporal signals: a method based on perturbation theory, Phys. Rev. E 60 (1999) 1350.
[16] R. Vautard, M. Ghil, Singular spectrum analysis in nonlinear dynamics, with applications to paleoclimatic time series, Physica D 35 (1989) 395.
[17] L. Sirovich, Turbulence and the dynamics of coherent structures, Parts I–III, Quart. Appl. Math. 45 (1987) 561.
[18] D. Armbruster, R. Heiland, E.J. Kostelich, KLTOOL: a tool to analyze spatiotemporal complexity, Chaos 4 (2) (1994) 421.
[19] A. Palacios, G.H. Gunaratne, M. Gorman, K.A. Robbins, Karhunen–Loéve analysis of spatiotemporal flame patterns, Phys. Rev. E 57 (1998) 5958.
[20] E. Stone, A. Cutler, Archetypal analysis of spatio-temporal dynamics, Physica D 96 (1996) 110.
[21] A. Politi, A. Torcini, Towards a statistical mechanics of spatiotemporal chaos, Phys. Rev. Lett. 69 (1992) 3421.
[22] H. Shibata, Quantitative characterization of spatiotemporal chaos, Physica A 252 (1998) 428.
[23] H. Xi, J.D. Gunton, Spatiotemporal chaos in a model of Rayleigh–Bénard convection, Phys. Rev. E 52 (1995) 4963.
[24] R.V. Cakmur, D.A. Egolf, B.B. Plapp, E. Bodenschatz, Bistability and competition of spatiotemporal chaotic and fixed point attractors in Rayleigh–Bénard convection, Phys. Rev. Lett. 79 (1997) 1853.
[25] D. Stassinopoulos, G. Huber, P. Alstrøm, Measuring the onset of spatiotemporal intermittency, Phys. Rev. Lett. 64 (1990) 3007.
[26] G.K. Harkness, J. Lega, G. Oppo, Measuring disorder with correlation functions of averaged patterns, Physica D 96 (1996) 26.

[27] P. Jung, Coherent structure analysis of spatiotemporal chaos, Phys. Rev. E 61 (2000) 2095.

[28] H.R. Schrober, E. Allroth, K. Schroeder, H. Müller-Krumbhaar, Dynamics of periodic pattern formation, Phys. Rev. A 33 (1986) 567.

[29] M.C. Cross, D.I. Meiron, Domain coarsening in systems far from equilibrium, Phys. Rev. Lett. 75 (1995) 2152.

[30] Q. Hou, S. Sasa, N. Goldenfeld, Dynamical scaling behavior of the Swift–Hohenberg equation following a quenching to the modulated state, Physica A 239 (1997) 219.

[31] D.A. Egolf, I.V. Melnikov, E. Bodenschatz, Importance of local pattern properties in spiral defect chaos, Phys. Rev. Lett. 80 (1998) 3228.

[32] F. Kwasniok, The reduction of complex dynamical systems using principal interaction patterns, Physica D 92 (1996) 28.

[33] S.G. Guan, C.-H. Lai, G.W. Wei, Characterization of spatiotemporal dynamics in a circular domain, unpublished.

[34] S.G. Guan, C.-H. Lai, G.W. Wei, Fourier–Bessel analysis of patterns in a circular domain, Physica D 151 (2001) 83.

[35] D. Permann, I. Hamilton, Wavelet analysis of time series for the duffing oscillator: the detection of order within chaos, Phys. Rev. Lett. 69 (1992) 2607.

[36] S. Thurner, M.C. Feurstein, M.C. Teich, Multiresolution wavelet analysis of heartbeat intervals discriminates healthy patients from those with cardiac pathology, Phys. Rev. Lett. 80 (1998) 1544.

[37] A. Marrone, A.D. Polosa, G. Scioscia, S. Stramaglia, A. Zenzola, Multiscale analysis of blood pressure signals, Phys. Rev. E 60 (1999) 1088.

[38] S. Boccaletti, A. Giaquinta, F.T. Arecchi, Adaptive recognition and filtering of noise using wavelets, Phys. Rev. E 55 (1997) 5393.

[39] L. Sirovich, Chaotic dynamics of coherent structures, Physica D 37 (1989) 126.

[40] U. Parlitz, G. Mayer-Kress, Predicting low-dimensional spatiotemporal dynamics using discrete wavelet transforms, Phys. Rev. E 51 (1995) R2709.

[41] C. Meneveau, Dual spectra and mixed energy cascade of turbulence in the wavelet representation, Phys. Rev. Lett. 66 (1991) 1450.

[42] L. Hudgins, C.A. Friehe, M.E. Mayer, Wavelet transforms and atmospheric turbulence, Phys. Rev. Lett. 71 (1993) 3279.

[43] R. Benzi, L. Biferale, E. Trovatore, Ultrametric structure of multiscale energy correlations in turbulent models, Phys. Rev. Lett. 79 (1997) 1670.

[44] J. Fröhlich, K. Schneider, Computation of decaying turbulence in an adaptive wavelet basis, Physica D 134 (1999) 337.

[45] T.J. Burns, S.K. Rogers, D.W. Ruck, M.E. Oxley, Discrete, spatiotemporal, wavelet multiresolution analysis method for computing optical flow, Opt. Eng. 33 (7) (1994) 2236.

[46] J.P. Leduc, J.M. Odobez, C. Labit, Adaptive motion-compensated wavelet filtering for image sequence coding, IEEE Trans. Image Process. 6 (6) (1997) 862.

[47] J.P. Leduc, F. Mujica, R. Murenzi, M.J.T. Smith, Spatiotemporal wavelets: a group-theoretic construction for motion estimation and tracking, SIAM J. Appl. Math. 61 (2) (2000) 596.

[48] S.J. Choi, J.W. Woods, Motion-compensated 3D sub-band coding of video, IEEE Trans. Image Process. 8 (2) (1999) 155.

[49] J.K. Chang, L. Huntsberger, Dynamic motion analysis using wavelet flow surface images, Pattern Recog. Lett. 20 (4) (1999) 383.

[50] Y. Meyer, Wavelets and Operators, Cambridge Studies in Advanced Mathematics, Vol. 37, Cambridge University Press, Cambridge, 1992.

[51] I. Daubechies, Orthonormal bases of compactly supported wavelets, Commun. Pure Appl. Math. 41 (1988) 909.

[52] I. Daubechies, Ten Lectures on Wavelets, CBMS-NSF Series in Applied Mathematics, SIAM, Philadelphia, PA, 1992.

[53] S. Mallat, Multiresolution approximations and wavelet orthonormal bases of $L^2(R)$, Trans. Am. Math. Soc. 315 (1989) 68.

[54] C.K. Chui, An Introduction to Wavelets, Academic Press, San Diego, CA, 1992.

[55] J.W. Cahn, J.E. Hilliard, Free energy of a nonuniform system. I. Interfacial free energy, J. Chem. Phys. 28 (1958) 258;
J.W. Cahn, J.E. Hilliard, Spinodal decomposition—a reprise, Acta Metall. 19 (1971) 151.

[56] J.D. Gunton, M.S. Miguel, P.S. Sahni, in: C. Domb, J.L. Lebowitz (Eds.), Phase Transitions and Critical Phenomena, Vol. 8, Academic Press, London, 1983, pp. 267–482.

[57] G.W. Wei, Discrete singular convolution for the solution of the Fokker–Planck equation, J. Chem. Phys. 110 (1999) 8930;
G.W. Wei, Discrete singular convolution for the sine-Gordon equation, Physica D 137 (2000) 247;
G.W. Wei, A unified approach for the solution of the Fokker–Planck equation, J. Phys. A 33 (2000) 4935.